5-2008

Correlation of NIS mRNA levels with radioiodide uptake in mammary tumors and non-tumor mammary glands of MMTV-infected mice

Stephen Schworer
College of William and Mary

Recommended Citation

Schworer, Stephen, "Correlation of NIS mRNA levels with radioiodide uptake in mammary tumors and non-tumor mammary glands of MMTV-infected mice" (2008). *Undergraduate Honors Theses.* Paper 806.
https://scholarworks.wm.edu/honorstheses/806

Correlation of NIS mRNA levels with radioiodide uptake in mammary tumors and non-tumor mammary glands of MMTV-infected mice

A thesis submitted in partial fulfillment of the requirement
for the degree of Bachelors of Science in **Biology** from
The College of William and Mary

by

Stephen Andrew Schworer

Accepted for ___________________________________

____
Eric L. Bradley, Director

____
Margaret S. Saha

____
Patty Zwollo

____
Lisa M. Landino

Williamsburg, VA
April 29, 2008

ACKNOWLEDGEMENTS

I would first like to acknowledge my great appreciation to Dr. Eric Bradley for giving me the opportunity to work in his lab for three and a half years and for giving me guidance and support in the lab and in the classroom. I would like to thank Dr. Margaret Saha for her endless hours of work in helping me to prepare this thesis. Without her, this end product would not have been possible. I greatly appreciate the contributions to this work by Dr. Nicholas Kenney, who taught me a great deal about mammary gland biology and performed many mouse dissections, in addition to providing his life lessons in the lab. The work on NIS immunohistochemistry and companionship in the lab from Eric Blue was invaluable during the past two years. I would also like to thank Jianguo Qian for his help in assembling gamma camera images for this project. Additionally, I would like to thank my fellow honors students in the Saha lab: Brittany Johnson, Kellyn Carrierfenster, Daniel Teasley, and Drew Hughes, as well as Matt Wester for their moral support and technical assistance throughout my project. Finally, I would like to thank my family for their guidance and support throughout this project.

This work was supported by the Undergraduate Biological Sciences Education Program Grant to the College of William & Mary from the Howard Hughes Medical Institute and by the Department of Defense Breast Cancer Research Program.

TABLE OF CONTENTS

Page

LIST OF TABLES

Page

LIST OF FIGURES

ABSTRACT

We have developed an in vivo non-invasive gamma camera imaging system which uses ^{125}I to detect functional iodide metabolism in mammary tumors. Iodide metabolism in these tumors is mediated by the sodium iodide symporter. The quantity and pattern of radioiodide uptake varies between mammary tumors. We have previously shown that localization of NIS protein expression reflects the radioiodide uptake in gamma camera images. In this study, we investigate whether expression levels of NIS mRNA in mammary tumors correlate with ^{125}I uptake pattern shown in gamma camera images. Our hypothesis is that NIS function in mammary tumors and non-tumor mammary glands is regulated primarily at the transcriptional level. To test this hypothesis, we quantified NIS mRNA levels using TaqMan real-time RT-PCR, and constructed a cRNA standard curve for quantification. The ratio of NIS to the housekeeping gene β-actin was compared to the intensity and pattern of mammary tumor radioiodide uptake as imaged by the gamma camera. In MMTV tumors, our results suggest that NIS is under both transcriptional and post-transcriptional control in this model for breast cancer. In separate tumors, we observed both positive correlation and no correlation between NIS mRNA level and radioiodide uptake. We also found that NIS mRNA levels were increased in non-palpable tumors in correlation with increases in radioiodide uptake, suggesting that an upregulation of NIS mRNA occurs in early tumor development.

INTRODUCTION

Overview

While the number of deaths resulting from breast cancer has dropped gradually over the past 15 years, it remains the most prevalent cancer in females (Jemal, 2007). In 2007, the number of new cases in the United States reached 178,480. Despite the decline in the breast cancer death rate, more than 40,000 women died from this form of cancer in the past year.

Early detection and diagnosis of breast cancer offers the best strategy to improve the odds of curing the disease (Benard, 2005). Imaging systems such as mammography and magnetic resonance imaging (MRI) are currently used for breast cancer screening and early detection. While these technologies create images displaying anatomical features of the breast, they lack the capacity to convey any functional information (Lyons, 2005). With the implementation of strategies such as positron emission tomography (PET) and gamma camera imaging, functional information about tumor physiology could be gathered (Benard, 2005). While PET conveys information on cell metabolism, effective diagnosis of breast cancer relies upon information regarding gene expression patterns and molecular alterations that cannot be obtained without targeting a breast cancer-specific ligand. One promising methodology for obtaining molecular images is using gamma camera imaging and radioiodide.

Gamma camera imaging has been employed previously for breast cancer imaging and detection (Schillaci, 2006; Brem, 2007). Imaging using a gamma camera measures low energy gamma rays for in vivo detection of iodinated compounds that display functional information of mammary tumor activity. We are currently using a mouse mammary tumor virus (MMTV)-infected mouse model to develop this system for early detection of tumor development and to investigate the relationship between heterogeneous uptake of ^{125}I and mammary tumor progression. The gamma camera developed by Bradley et al. (2006) has resolution which is sufficient to detect the presence of non-palpable tumors. Additionally, as tumors develop distinct patterns of radioiodide uptake have been observed. Ultimately, we aim to relate this heterogeneity of iodide uptake patterns to differences in gene and protein expression within mammary tumors.

Iodide uptake in mammary tumors relies on expression of the sodium iodide symporter (NIS), a transmembrane protein that cotransports sodium and iodide into cells (Tazebay, 2000). This study investigates how levels of NIS mRNA levels correlate to both the total amount and pattern of radioiodide uptake in MMTV-induced mammary tumors. To provide the necessary background for the presentation of this study, the remainder of this chapter will discuss (1) the biology of MMTV-induced mammary cancer, (2) the modalities used in breast cancer imaging, genes currently used as markers for breast cancer development, and (3) the current usage of molecular imaging in breast cancer detection and diagnosis.

Mouse Mammary Tumor Virus – A Mouse Model for Breast Cancer

The mouse mammary tumor virus (MMTV) is a retrovirus, inserting its DNA into the host genome and insertionally activating host proto-oncogenes (Cardiff, 2007). MMTV exists in both exogenous and endogenous forms (Golovkina, 1997). Exogenous, or milk-borne, MMTV is transmitted from infected mice to newborns through the breast milk during nursing. An exogenous MMTV inserts its provirus into the host genome and leads to activation of downstream oncogenes. Nearly all laboratory mice contain endogenous MMTVs within their genomes. These endogenous MMTVs are often inactive due to regulatory or coding region mutations. Proviral expression of inserted exogenous MMTV or functional endogenous MMTV is transcriptionally regulated by a long terminal repeat (LTR) sequence. The MMTV-LTR contains hormone response elements within its sequence that drive MMTV expression, driving downstream activation of host oncogenes (Cardiff, 2007). The oncogenes which can be activated by insertion of MMTV include ras, myc, erbB, Fos, and myb. A mouse will develop mammary tumors upon activation of the MMTV-LTR in mammary gland tissue and downstream activation of host oncogenes.

The MMTV mouse is a widely used model of breast cancer because of the similarity between mouse and human mammary glands and the ability for MMTV mice to spontaneously develop tumors (Cardiff, 1999). MMTV-infected mouse models have been used in the description of the natural history of neoplasia, oncogenic viruses, endocrinology, and neoplastic progression (Cardiff, 2007). The model has also been recently used in the study of signaling in breast cancer, including NIS signaling (Politi, 2004; Knostman, 2004) We have used this proven model in the development of an imaging system that aims to use the molecular characteristics of mammary tumors to further understanding of early diagnosis of breast cancer.

Breast Cancer Imaging

Because early diagnosis is an important step to ensure the most effective treatment of breast cancer, a strong focus has been placed on imaging technologies for screening and diagnosis the disease (Benard, 2005). Imaging strategies currently implemented for widespread clinical use, including mammography and MRI have been useful in breast cancer diagnosis but additional techniques can significantly improve diagnostic imaging. While the anatomical images created by mammography and MRI are useful, functional images through PET and gamma camera imaging provide more specific information (Benard 2005; Quon, 2005). Gamma camera imaging additionally offers the potential for molecular imaging using ligands specific to breast cancer (Torigian, 2007). Using a combination of these technologies will greatly improve the current ability for early diagnosis of breast caner.

Mammography

Mammography has been used as preferred method of screening for breast cancer for over 40 years (Elmore, 2005). This imaging modality uses ionizing radiation in the form of X-rays to record the variations in density of the tissue through which the radiation passes (Esserman, 2002). This anatomical image can display dense masses that have the potential to be abnormal tissue or calcifications that signify the development of breast cancer. However, because mammography measures only the density of breast tissue, the image does not contain any functional information about the breast. Because of its lack of specificity, the mammogram has difficulty detecting abnormalities in dense breasts, and leads to false positive diagnoses.

Magnetic Resonance Imaging

MRI provides an imaging modality with higher sensitivity and conveys more functional information than mammography, but does not provide any molecular or metabolic information (Esserman, 2002; Lyons 2005). The signal for MRI is generated by measuring protons in H_2O molecules using radiowaves (Esserman, 2002). An image is produced by visualization of the differences in H_2O content in tissues, distinguishing between tissue types. In breast cancer MRI, a contrast agent consisting of a paramagnetic cation probe often containing gadolinium is necessary to enhance the signal where it accumulates (Esserman, 2002; Lyons 2005).

MRI creates anatomical images, with a resolution of approximately 25 µm (Lyons, 2005). Highly vascularized dense tissue images particularly well with MRI. However, a significant limitation to the use of MRI for gathering functional information about a mammary tumor exists in its inability to provide any specific molecular information (Hylton 2005). Because of its reliance on measuring only relative water content, MRI lacks molecular specificity, and therefore possesses the potential to give high percentages of false positive diagnoses (Wright 2005). The high cost of MRI also contributes to its limitations in widespread clinical use.

While MRI in clinical use is limited to anatomical imaging, its use in noninvasive in vivo mouse imaging is expanding to include functional information about tissue physiology (Lyons, 2005). While traditional MRI relies on non-targeted probes, new advances utilize probes which can localize specifically to tumor cells. Examples include using cross-linked iron oxide to detect overexpression of the MUC1 promoter in tumors and using an iron oxide-transferrin chelate to detect overexpression of the transferrin receptor. These examples display the potential for an improved level of specificity and ability to image tumor function in the use of MRI.

Positron Emission Tomography

Positron emission tomography detects the annihilation of photons from positron-emitting radioisotopes such as ^{15}O, ^{13}N, ^{11}C, and ^{18}F (Benard, 2005). PET imaging with [^{18}F] fluorodeoxyglucose (^{18}F-FDG) is used commonly in cancer prognosis in many cancer centers across the United States (Benard, 2005; Quon, 2005). ^{18}F-FDG detects cancer through its incorporation into cells at a rate proportional to that of glucose metabolism (Nahmias, 2002; Quon, 2005). The radioisotope follows the glycolysis pathway and is phosphorylated by hexokinase (Benard, 2005). This phosphorylated ^{18}F-FDG cannot be metabolized further by the cell and is trapped at this stage of the pathway. In cancer, where glycolytic rate is increased compared to normal tissue, the phosphorylated ^{18}F-FDG trapped in these cells is significantly greater than the surrounding tissues, allowing detection using PET based on the increased positron emission in these cancer tissues (Quon, 2005).

The benefit of PET imaging over mammography or MRI is found in its capability to acquire functional information of glucose metabolism within a tumor (Quon, 2005). While mammography and MRI can detect abnormalities in breast tissue, PET can differentiate cancerous tissue from normal tissue by tracing functional rather than morphological abnormalities. Considering this information, PET imaging demonstrates potential for use in diagnosis, staging, restaging, and monitoring the treatment of breast cancer (Schoder, 2007).

However, PET imaging only demonstrates changes glucose metabolism, not gene expression information that will lead to diagnosis and prognosis of the type of breast cancer (Benard, 2005). False negatives result both from the poor capability of ^{18}F-FDG PET to image noninvasive breast cancer and the low detection rate in small tumors (0.4-1.5 cm) (Quon, 2005). False positives are detected by PET in benign inflammations and fibroadenomas of the breast. While PET imaging using ^{18}F-FDG signifies an improvement in terms of the ability to functionally image breast cancer, its limitations in specificity and sensitivity suggest the need for an additional imaging technology.

Gamma Camera Imaging Using the Sodium Iodide Symporter

Gamma ray emitting radioisotopes such as ^{123}I, ^{125}I, and ^{131}I injected into a subject can be detected using gamma cameras to image molecular events as the radioiodide is taken up by tissues that express the sodium iodide symporter (Schipper, 2007). This technology provides the ability for repeatable, non-invasive imaging which monitors functional activity through radioiodide uptake (Dingli, 2003).

Gamma camera imaging using radioiodide provides many significant advantages over ^{18}F-FDG PET scans. Gamma camera technology is more available to hospitals than PET scanners (Dingli, 2003). In addition, ^{125}I and other radioactive iodide isotopes are readily commercially available at a low cost, while PET radiotracers require sophisticated onsite radiochemistry to produce (Dingli, 2003; Weisenberger, 2003). The long half-life (60 days) of ^{125}I also allows tracking of biological processes in animals, which cannot be accomplished using short half-life radiotracers such as ^{18}F used in PET. Also, the use of radioiodide is already approved for medical use by the FDA, easing the transition to use in clinical practice (Dingli, 2003).

The gamma camera for small animal imaging developed by Bradley et al. (2006) improves on the current resolution capabilities of gamma cameras used for cancer imaging. Currently available gamma cameras can produce images with a range of 5-10 mm resolution (Dingli, 2003). The compact gamma camera for biological imaging described in Bradley et al. (2006) has the capacity to produce images with a resolution of 2.5 mm using the radioisotope ^{125}I. With high resolution, non-invasive functional imaging at low cost, this gamma camera possesses the capacity for early detection of breast cancer by monitoring radioiodide uptake through NIS.

Breast Cancer Markers and Reporter Genes

With its ability to develop in vivo high resolution images, our system for gamma camera imaging has the potential to use radiolabeled ligands that reveal molecular and functional information about a tumor. Many genes are overexpressed in breast cancer, so determining such overexpression can offer valuable information about the phenotype of the cancer, which has implications on treatment strategy and probability of recurrence and metastasis (Kapp, 2006). The following discusses some particularly important ligands which are overexpressed in breast cancer cells, and provide functional information of tumor activity.

Estrogen Receptor

The estrogen receptor alpha (ERα) is coded for by the Esr1 gene, and is expressed in approximately 75% of invasive breast cancers (Fowler, 2007; Allred, 2004). ERα is a nuclear receptor that binds the sex steroid hormone, estrogen and directly activates an estrogen responsive element on DNA (Ikeda, 2004). Esr1 and ERα overexpression has been demonstrated in benign breast lesions, carcinomas *in situ,* and invasive breast carcinomas (Fowler, 2007). In each of these samples, ERα expression contributed to tumorigenesis and cancer cell proliferation. Mammary tumors that are well-differentiated, responsive to endocrine therapy, and have a generally favorable prognosis are correlated with ERα expression. Because of its prognostic value, determination of ERα expression provides valuable information about tumor progression and development. This information would be useful in our radioiodide imaging system.

Amphiregulin

Amphiregulin (AREG) is an autocrine growth factor and a member of the epidermal growth factor family of proteins that activates the epidermal growth factor receptor (EGFR) (Normanno, 1994; Ma, 1999; Ciarloni, 2006). AREG expression is documented in normal and malignant epithelial tissues and has the potential to either stimulate or inhibit cell growth depending on the presence of other growth factors (Normanno, 1994). In mammary tumorigenesis, AREG has been implicated as a major element in estrogen-induced breast cancer cell proliferation (Ciarloni, 2006). In addition to its role in cell proliferation, AREG has also been shown to play a role in endothelial-mesenchymal transition (EMT) in human kidney cells as well as in tumor angiogenesis

(Lee, 2007; Ma, 1999). Because of the above factors and its enhancement of tumorigenicity in breast cancer cell lines, the use of AREG as a therapeutic target and prognostic indicator is promising. As a prognostic indicator of tumor progression and estrogen-induced tumor cell proliferation, the use of ^{125}I-tagged AREG as a marker for breast cancer development is promising for our small animal gamma camera detector system.

Sodium Iodide Symporter

The sodium iodide symporter (NIS) is a plasma membrane glycoprotein with an extracellular amino terminus and intracellular carboxyl terminus, and contains 13 putative transmembrane domains (Smanik, 1997; Levy, 1998). The gene that encodes NIS consists of 15 exons separated by 14 introns. Three potential N-linked glycosylation sites exist, one on the seventh extramembrane loop and two on the thirteenth extramembrane loop. NIS is endogenously expressed in thyroid, gastrointestinal tract, salivary gland, and lactating mammary gland where it allows the cellular uptake of iodide (Dai, 1996; Tazebay, 2000). Two sodium ions and one iodide ion are cotransported across the cell membrane through NIS (Carrasco, 1993). The transmembrane sodium gradient generated by the sodium/potassium ATPase acts as a driving force for iodide uptake and can be inhibited by perchlorate. According to Tazebay et al. (2000), mammary gland NIS and gastric NIS, yield the same peptide map as thyroid NIS and the clones of human cDNAs of thyroid, mammary gland, and gastric NIS are in agreement (Spitzweg, 1998). Mouse NIS was cloned in 2001, and found to have 95% identity with rat NIS and 81% identity with human NIS (Perron, 2001). Differences between human and mouse NIS efficiency of iodide transport have been documented in transfected human embryonic kidney 293 cells (Dayem, 2008). Localization studies of human NIS compared with mouse NIS additionally found that mouse protein was located predominately on the cell membrane, while approximately 40% of cells transfected with human NIS demonstrated intracellular protein localization.

Tazebay et al. (2000) established that ^{125}I was concentrated in lactating mammary gland in rats, but not in surrounding skeletal muscle of the same rat or in mammary glands form non-lactating rats. Using antibody for rat thyroid NIS, a single band of 75-kDa was detected in immunoblot analysis of rat lactating mammary gland. Immunoblot analysis also showed that NIS expression in rat mammary gland varies in different physiological stages (Cho, 2000; Tazebay, 2000). Mammary gland NIS protein expression begins in late pregnancy, continues through lactation, and is abolished 48h after suckling ceases. With re-initiation of suckling, NIS expression levels increase. Immunohistochemical staining demonstrated that NIS is located on the basolateral membrane of alveolar epithelial cells, which are much more developed in the lactating mammary gland than in glands of virgin individuals. RT-PCR analyses on rat mammary tissues produced positive results for non-lactating as well as lactating tissues, indicating that while protein is not present at detectable levels, NIS mRNA is constitutively expressed (Tazebay, 2000; Spitzweg, 1998). Perron et al. (2001) used semi-quantitative RT-PCR studies of mouse NIS to show that lactating mammary gland expressed significantly more NIS mRNA than virgin, pregnant, or involuting mouse mammary glands, Immunoblot analysis revealed that hormonal regulation of rat NIS protein expression is mediated by prolactin, oxytocin, and β-estradiol (Cho, 2000; Tazebay, 2000), but the pathways are not well understood (Riesco-Eizaguirre, 2006). Oxytocin alone, but not in combination with prolactin, induced NIS expression (Tazebay, 2000). This finding suggests that NIS can be expressed in the mammary gland independently of gestation- and lactation-related changes.

NIS in Breast Cancer

NIS expression and function in breast cancer was first documented by Tazebay et al. (2000). Functional expression of NIS was demonstrated in mammary tumors of two female transgenic mice, one with an activated *Ras* oncogene and the other overexpressing the *Neu* oncogene (Tazebay, 2000). Both genes were under transcriptional control of an MMTV promoter/enhancer. Using scintigraphic imaging, $^{99m}TcO_4$ accumulation was reported in mammary gland adenocarcinomas of both mouse strains. Immunoblot analysis showed NIS protein expression in these mammary tumors (Tazebay, 2000). Contralateral nontumoral mammary glands showed no NIS expression upon immunoblotting. Functional NIS expression was also demonstrated through ^{125}I and ^{131}I uptake studies in human primary breast tumors (Moon, 2001). Expression of NIS mRNA in human breast carcinomas was demonstrated by RT-PCR (Kilbane, 2000). MMTV-PyVT transgenic mice with spontaneously developing tumors were also shown to have NIS mRNA expression by RT-PCR (Kogai, 2004). The localization of NIS protein in breast cancer differed from its exclusive expression on the basolateral surface of alveolar cells in lactating mammary glands. When a group of seven transgenic mouse models showed positive immunohistochemical staining for NIS in mammary tumors, some showed staining on only the plasma membrane, while others expressed NIS intracellularly (Knostman, 2004). *In situ* staining by Tazebay et al. (2000) also demonstrated both plasma membrane and intracellular staining in malignant breast cells.

Sodium iodide symporter expression studies in human breast cancer tissue have shown that NIS is frequently expressed in mammary carcinomas, suggesting that the NIS could be used as a marker for this type of breast cancer. The high prevalence of NIS expression in mammary carcinomas (80%) and its absence in normal tissue compared with the 33% prevalence of a current breast cancer marker, Her2/*neu,* suggests that NIS expression and radioiodide uptake may be a more effective breast cancer marker in some cases than current methods (Dohan, 2003a). Additional immunohistochemical studies have shown that a significant percentage of mammary carcinomas are positive for NIS. IHC analysis of 371 human breast cancer cases showed positive *in situ* staining for NIS in 88% of ductal carcinomas and 76% of invasive carcinomas while 87% of normal breast samples were negative (Wapnir, 2003). In a study of human breast tissues, 87% of 23 invasive carcinomas and 83% of six ductal carcinomas *in situ* expressed NIS compared with 23% of noncancerous samples in the vicinity of the tumors (Tazebay, 2000). While these studies suggest a strong correlation between breast cancer development and NIS expression, Moon et al. (2001) found a weaker correlation between correlation between functional NIS shown by $^{99m}TcO_4$ accumulation and NIS mRNA expression. The relationship was tested in 25 patients with four out of 25 mRNA expressing tumors possessing functional uptake. Although Moon’s percentage of functional NIS is significantly lower than NIS protein expression, a review by Dohan and

Carrasco suggests that these results are still highly meaningful because iodide uptake in the thyroid was not blocked in these patients (Dohan, 2003b). They suggest that a larger proportion of radioiodide uptake could occur in the mammary gland tumors or metastases if thyroid radioiodide uptake was suppressed by T_3 (Wapnir, 2004).

Relationship between expression of NIS and the Estrogen Receptor

In order to understand more specifically the characteristics of cancers that express NIS, the estrogen receptor (ERα) and associated genes have been investigated in breast cancer cell lines and in human breast cancer tissue samples and compared with the presence of NIS. According to Kogai et al. 2000, ^{125}I uptake, as well as NIS expression, in MCF-7 cells is present, but small at baseline. Uptake of ^{125}I did not occur in ER-negative MDA-MB-231 breast cancer cells or in MCF-12A normal breast cells. A more comprehensive study of breast cancer cell lines by Alotaibi in 2006 showed by RT-PCR that the ER+ cell lines BT-474, T-47D, and MCF-7 expressed NIS, as well as the ER- cell line, BT-20. Only ER positive cell lines were capable of increased NIS expression following trans-retinoic acid (tRA) treatment.

In human breast cancer samples, both ER-positive and ER-negative tissues show NIS expression in real-time RT-PCR (Tanosaki, 2003) and immunohistochemistry (Wapnir, 2004) analysis. Twenty-two human breast cancer samples, among which eleven were ER-positive, were compared with MCF-7 human breast cancer cells. Only three of these tissue samples showed NIS activity above that of MCF-7. Of these, two were ER-positive and one was ER-negative. Wapnir et al. (2004) examined 27 patients with metastatic breast cancer who underwent $^{99m}TcO_4$ or I-123 scans, and correlated results with IHC findings in 23 of these cases. Of the 23 cases studied, eight stained positive for NIS (34.8%). Three of the nine metastatic samples and five of the 14 primary tissue samples that were collected stained positive for NIS. Seven of the eight positive NIS tissues were ER-negative, indicating that NIS is expressed in both ER-positive and ER-negative tissues despite many ER-negative breast cancer cell lines lacking NIS expression. These findings suggest that further studies of NIS expression in ER-positive and ER-negative breast cancer tissues are required to more completely understand the relationship between ER expression and NIS-regulated iodide uptake in breast cancer.

Molecular Imaging of Breast Cancer

Molecular imaging in breast cancer utilizes target molecules, such as those mentioned above, with specific roles in the development of the disease. This type of imaging offers more specific targets than the structural/anatomical imaging techniques such as mammography and MRI (Torigian, 2007). These molecular targets can provide information to assist in prognosis or treatment of the cancer, which structural imaging cannot provide without a biopsy. Molecular imaging with specific cellular targets can measure specific cellular events such as proliferation and apoptosis which surpasses imaging modalities such as FDG-PET (Mankoff, 2004). This analysis of tumor activity examines specific events within the tumor, rather than only providing information on how the tumor metabolizes glucose. Overall, the potential for molecular imaging to offer a quantitative measurement of a target, while simultaneously having the capacity to identify resistance factors for treatment and measure treatment response reveals the promise of this imaging strategy for future diagnosis and treatment of breast cancer.

Molecular Imaging Strategies in Breast Cancer

Current strategies in molecular imaging which employ PET imaging include cell proliferation, apoptosis, and estrogen receptor imaging (Mankoff, 2004; Torigian, 2007). Cell proliferation imaging measures the uptake of nucleosides incorporated into nucleic acid synthesis using the nucleoside analogue 3’-deoxy-3’-^{18}F-fluorothymidine (FLT). This tracer, similar to ^{18}F-FDG becomes phosphorylated and cannot be metabolized further, allowing for imaging using PET. While FLT is specific to cellular-proliferation activity, its sensitivity is less than that of FDG-PET for the detection of cancer. This suggests that the current system using FLT is extremely useful in monitoring anti-proliferation treatment, but lacks the sensitivity to be used as a cancer detection system.

Imaging of apoptosis within tumors can be achieved using a either a ligand labeled with ^{125}I to be detected with SPECT or ^{18}F to be detected with PET radioisotope that can be detected using SPECT or PET imaging. Annexin V can be labeled and imaged when it binds to phosphatidylserin (PS). PS moves the surface of the cell membrane when apoptosis occurs, at which point Annexin V binds and can be detected using radionuclide imaging Torigian, 2007).

As mentioned above, the estrogen receptor is an important target for breast cancer therapy, and detecting this molecule in vivo is particularly useful because it is screened for often in biopsies. Using the estrogen analogue 16α-^{18}F-fluoroestradiol-17β (FES) with PET, the activity of the estrogen receptor can be non-invasively imaged in vivo (Mankoff, 2004). It has also been demonstrated that this FES-PET imaging can be accurately quantified, providing information on the level of ER expression. FES-PET provides the potential to monitor and prescribe treatment protocols based on the presence of the ER as assessed in vivo.

NIS as a Reporter Gene

NIS has potential as a reporter gene for breast cancer as well as a therapeutic gene. The ability of this transmembrane protein to cotransport sodium with a multitude of different anions contributes to its versatility and usefulness. In addition to I^-, NIS can also transport ClO_3^-, SCN^-, $SeCN^-$, NO_3^-, Br^-, $TcO4^-$, RhO_4^-, and ^{211}At into cells (Dingli, 2003). In Dingli et al. (2003), NIS in the form of a replication competent measles virus (MV-NIS) was used to trace ^{123}I uptake in myeloma xenograft tumors in mice. These tumors were imaged after 17 days to allow for MV-NIS proliferation with a gamma camera, and displayed prominent radioiodide uptake in the regions of the myeloma tumors. Exogenously introduced NIS was successfully demonstrated as a breast cancer reporter gene by Schipper et al. (2007) and Dwyer et al. (2005). Schipper's group measured radioiodide uptake in mouse neuroendocrine xenograft tumors with stably transfected NIS. These mice were then imaged with gamma camera and SPECT imaging to detect regions of radioiodide uptake. Dwyer performed a similar analysis using a NIS expression driven by a MUC-1 promoter in breast cancer xenografts.

In studies of ER-positive breast cancer cell lines such as MCF-7, NIS induction through trans- or 9-cis- retinoic acid treatments have been shown to increase mRNA and protein expression levels substantially (Kogai, 2000; Kogai, 2004; Tanosaki, 2003). Kogai showed that tRA stimulation of MCF-7 cells led to an increase of NIS mRNA expression using Northern blot analysis and an increase in protein expression by western blotting. The same studies on ER-negative MDA-MB-231 cells expressed low levels of NIS protein initially, which increased very slightly upon tRA treatment. MCF-7 xenograft tumors grown in female SCID mice and treated with tRA show ^{125}I uptake in vivo, while no uptake occurs without tRA treatment. RT-PCR and western blots showed increased levels of mRNA expression and protein expression, respectively, upon tRA treatment in MCF-7 xenograft tumors.

Potential of Molecular Imaging

Molecule-specific non-invasive in vivo imaging presents an opportunity to obtain quantitative information regarding physiological processes that cannot be achieved with strictly anatomical imaging technologies. Continued study of molecular imaging ligands and advances in imaging technology to improve image resolution will likely impact the ability to detect tumors early in development, monitor therapy, and develop a prognosis using non-invasive techniques (Torigian, 2007). The overall goal of the field of molecular imaging is to correlate imaging with molecular mechanisms, eventually gaining the capacity to image at the molecular level and to produce an image predictive of a molecular signature. Through our study of NIS in breast cancer, we aim to combine gamma camera imaging with molecular biology for the early detection of mammary tumors and to determine if radioiodide uptake correlates with NIS protein and mRNA expression. We will then determine if these images possess predictive value for breast cancer diagnosis or prognosis.

Hypothesis and Predictions

In our current experimental approach, we are using gamma camera imaging of the early development of mammary tumors by measuring and visualizing radioiodide uptake in MMTV-induced mammary tumors via endogenous expression of NIS. We are examining if NIS mRNA levels correlate with the intensity and pattern of radioiodide uptake in mammary tumors. Our working hypothesis is that NIS expression in mammary tumors is regulated primarily at the transcriptional level. From this hypothesis, we predict that tumors (or regions of tumors) with higher levels of iodide uptake, as revealed by the gamma camera image, will have correspondingly higher levels of NIS mRNA.

MATERIALS AND METHODS

Animals and Gamma Camera ^{125}I Imaging

The mouse model used in this study was from the strain C3H (Jackson Laboratories), and contained an endogenous MMTV. This model spontaneously developed tumors specific to the mammary glands. We used C57BL/J6 mice in studies of radioiodide uptake in lactating, multiparous, and nulliparous mice for comparison with data from MMTV mice. All mouse studies were carried out using protocols approved by the College of William & Mary animal committee.

Mouse imaging was performed following an injection of 14 μCi of Na^{125}I in 0.10 ml 0.9% saline into the femoral biceps of the left rear leg as described in Bradley et al. (2006). The gamma camera for small animal imaging was described previously (Weisenberger, 2003; Bradley, 2006; Hammond, 2007) and will be briefly described here. The detector consists of a Hamamatsu R3292 position-sensitive photomultiplier tube and is air coupled to a pixilated array of CsI scintillating crystals. A 3.0 mm thick CuBe parallel hole collimator with 0.2 mm square holes separated by 0.11 mm septal walls was placed in contact with the scintillator. The system provides an effective special resolution of 2.5 mm (FWHM) on contact with the detector surface. Data collection performed as described in Hammond et al. (2007) with additional analysis of region of interest (ROI) data. Data were collected in five minute time-cuts over a period of 60 minutes using KMAX data acquisition software on a Macintosh G4 system to record the time and energy of each photon emitted. These data were examined by ROI analysis by defining regions incorporating tumors and mammary glands without the inclusion of surrounding tissues that also showed radioiodide uptake. An IDL-based program was used to create an array of the total number of counts per pixel in each ROI, allowing the size of the tumor to be defined as well as displaying its pattern of radioiodide uptake.

RNA Extraction and DNaseI Treatment

Total RNA was isolated from frozen tissues by RNeasy maxi kits following the manufacturer's protocols (QIAGEN, Valencia, CA) with tissue homogenization performed using a Tissue Tearor rotor homogenizer (Biospec Products, Inc., Bartlesville, OK). To assess RNA quality, 10 µl of total RNA from each extraction was added to 2 µl 6X dye components and was separated on 1.2% agarose gel stained with ethidium bromide. RNA samples were only used for further analyses if two distinct bands appeared, signifying intact 28S and 18S rRNA.

Following total RNA elution, DNA-free DNaseI treatment was applied to all samples of extracted total RNA (Ambion, Foster City, CA). For each DNaseI treatment, 10 µg of total RNA was combined with 1 µl of DNaseI at a concentration of 2 U/µl according to manufacturer protocol for normal treatment. Concentration of RNA was determined prior to and following DNaseI treatment using a NanoDrop Spectrometer with NanoDrop 3.5.2 software. DNaseI treated RNA was stored at -80°C.

Reverse Transcriptase PCR

cDNA Synthesis

DNaseI-treated RNA samples were reverse-transcribed using a Bio-Rad iScript cDNA Synthesis kit (Hercules, CA) following the manufacturer's protocol with the following modifications. For each reaction, 1 µg of RNA template was added to the reverse-transcription reaction and incubated in a Bio-Rad iCycler for 5 minutes at 25°C, 60 minutes at 42°C, and 5 minutes at 85°C. A reaction lacking reverse transcriptase was also performed for each RNA sample reverse-transcribed to be used as a negative control in RT-PCR. The cDNA products were stored at -20°C until further use.

Primer Design and Handling for non-quantitiative RT-PCR

Intron-spanning sense and anti-sense primers were designed using Primer3 software (http://frodo.wi.mit.edu/). NCBI sequence information was entered into Primer3 software and primers were developed using the following parameters. Primer size between 18 and 27 base pairs was required, with 20 base pairs as the optimal molecular size, which is long enough to ensure sequence specificity while short enough to preventing mismatch pairing. This allows for high efficiency in annealing to the template. Primer melting temperature (Tm) and GC content were specified within the ranges of 53-60°C and 20-80%, respectively. Upon entering these specifications into Primer3 software, typically 2-4 sense/anti-sense primer combinations for each gene resulted. In the case of multiple primer set results, the first criteria for selection was whether the region of amplification crossed an exon-intron barrier. Only primer sets that crossed exon-intron barriers were used in RT-PCR. Exon-intron barriers were determined using NCBI sequence information. Primer sequences were then entered into an NCBI BLAST search (http://www.ncbi.nlm.nih.gov/BLAST/) to confirm high specificity for the gene of interest. (Table 1) If multiple primer sets matched these criteria, those with the lowest sequence identity with related genes expressed in *Mus musculus* were chosen.

Primers were manufactured by Integrated DNA Technologies (Coralville, IA) and shipped in lyophilized form. These were brought up in 1X Tris-EDTA (TE) to create 1 mM stocks and diluted to 100 µM and 10 µM stocks with nuclease-free H_2O. Primer 1mM stocks were stored at -80°C and dilutions were stored at -20°C.

Polymerase Chain Reaction

PCR was performed using Taq polymerase (New England Biolabs, Beverly, MA) and assembled and cycled under the following conditions. For each 50 µl reaction, 5 µl of 10X Thermopol buffer (New England Biolabs) which contains 2 mM of Mg^{2+} in the 1X dilution, 1 µl 40 mM dNTP mix (Promega, San Luis Obispo, CA) and nuclease-free H_2O were assembled in a master mix and an aliquot was transferred to 0.2 ml PCR tubes. To each tube, 2.5 µl of the 10 µM dilution of both forward and reverse primers to a concentration of 500 nM and 1 µl cDNA template were added. The samples were then placed in a Bio-Rad iCycler and incubated at 94°C for 5 minutes. Following this hot start, 0.25 µl Taq polymerase (New England Biolabs) was added to each reaction. The iCylcer protocol then performed 40 cycles of denaturation at 94°C for 30 seconds, annealing at 64°C for 1 minute, and extension at 72°C for 2 minutes, followed by a final extension at 72°C for 7 min. Negative controls lacking reverse-transcriptase in cDNA synthesis were performed for each PCR.

PCR products were analyzed by separation based on molecular size on a 1.2% agarose gel and stained with ethidium bromide. Gels were visualized under UV light using the Alpha Innotech (San Leandro, CA) FluorChem HD2 detection system.

TaqMan Quantitative Real-time PCR

Primer and Probe Design and Handling for qRT-PCR

Primers and probes for TaqMan quantitative real-time PCR were designed using Beacon Designer version 7.0 (Premier Biosoft, Palo Alto, CA). The sequences for NIS and β-actin were accessed from NCBI and entered into the Beacon Designer software for primer and TaqMan probe design for each gene of interest. Beacon Designer performs two searches to detect regions of each gene to avoid in primer/probe design: those that could form secondary structure and those that share similar sequences with other genes. Secondary structures were analyzed at a folding temperature of 55°C. Any self-folding that involved a stretch of fewer than 10 nucleotides was not considered a problem in design. An NCBI BLASTn search was then performed to determine regions of homology between the gene of interest and other *Mus musculus* genes to prevent non-specific amplification.

Beacon Designer then provides the option to perform a search for TaqMan primer/probes using its default settings for primer length (20-24 nucleotides), primer Tm (59 +/- 2°C) , amplicon length (75-150 base pairs), probe length (20-24 nucleotides), and probe Tm ([primer Tm + 10] +/- 2°C). After obtaining results from these searches for each NIS and β-actin, the “best” probes based on the rating number derived from the program’s algorithm were further analyzed using specifications for real-time PCR outlined by Dorak (2006) to choose an optimal primer/probe set. Beacon Designer displayed seven “best” results for NIS and five for β-actin. First, if possible, primers were selected to produce an amplicon which crosses an exon-intron barrier. This case was possible with a probe designated “best” for NIS PCR; however it was not possible for β-actin. Prioritization of primer selection was then based on physical properties of primers that were paired with "best" rated probes. Optimal Tm is defined by Dorak as between 58-60°C, and primer sets with similar Tm values will have comparable efficiencies during the PCR. The Tm of the probe was chosen to be as close to a 10°C higher Tm than the corresponding primers. The ideal GC% for primer/probe selection is between 30-80%. By keeping GC% within this range, the use of high annealing temperatures or cosolvents with the primers is not necessary. In both primer and probe design, choices containing runs of four or more guanine nucleotides were discarded. The amplicon size was also controlled in primer design to an optimum between 50-150 base pairs. This smaller size facilitates a more efficient PCR, and therefore more consistent results. The parameters of the selected primer/probe combinations are found in Table 2.

Primers and probes for TaqMan quantitative real-time PCR were purchased from Applied Biosystems (Foster City, CA). Primers were received at a concentration of 100 µM and suspended in 1X TE. A 100 µl aliquot of the stock primer solutions were further diluted in nuclease-free H_2O to a concentration of 12.5 µM. Both NIS and β-actin TaqMan probes were labeled on the 5' end with a 6FAM fluorophore and a 3' TAMRA quencher. The 100 µM stock of probe was diluted 1/20 to make 5 µM aliquots, all of which were stored at -20°C.

Generation of cRNA Standard

To create a cRNA standard for quantification of one-step real-time PCR transcripts, a PCR product of each gene of interest was cloned, transformed, linearized, and in vitro transcribed. For cloning and bacterial transformation, the TOPO TA cloning kit (Invitrogen, Carlsbad, CA) was used following the manufacturer's protocol for OneShot chemical transformation using DH5α-T1 competent cells into a pCRII-TOPO vector. Cells were plated on LB plates containing 50 µg/ml ampicillin at volumes of 30, 60, and 100 µl. Single bacteria colonies were picked and cultured overnight. DNA was purified from bacteria cultures using Wizard Plus SV Miniprep DNA Purification System (Promega) following the manufacturer's protocol. To determine if purified DNA incorporated the desired insert, a 20 µl EcoRI restriction enzyme digest was performed on each sample of purified DNA and separated on a 1.2% agarose gel. For all samples that contained the a band of the molecular size of the desired insert, 50% glycerol stocks of overnight bacteria culture were made and stored at -20°C. Plasmid DNA was then sequenced using the ABI 3100-Avant Genetic Analyzer (Applied Biosystems). ABI BigDye 3.1 sequencing reactions were prepared according to the manufacturer's protocol, followed by ethanol precipitation containing 125 mM EDTA. Pelleted DNA was resuspended in ABI Hi-Di formamide and sequenced according to the manufacturer's protocol for ABI 3100-Avant sequencing. BLAST nucleotide searches were performed on successful sequences to confirm the insertion of the entire insert within the plasmid DNA. Only plasmid DNA containing insert sequences of 100% identity to the published sequence for the gene of interest as well as containing the PCR primers used for insert amplification were used for further analysis.

In preparation for DNA purification, bacteria from glycerol stocks of samples that had been sequenced and confirmed to have incorporated the insert into plasmid DNA were grown overnight in 150 ml LB broth containing 50 µg/ml ampicillin. Plasmid DNA was purified from this bacterial culture using a Bio-Rad Midiprep kit according to manufacturer's protocol with the following modifications. During the initial centrifugation of overnight culture, three spins containing 50ml of culture each were performed for 10 minutes at 7000 RPM. Also, the DNA elution step was performed with 300 µl of sdd H_2O rather than the 600 µl recommended by the manufacturer. The concentration of purified DNA was then measured using a NanoDrop spectrophotometer.

Plasmid DNA was linearized for in vitro transcription using the protocol for preparation of linearized template DNA from plasmid DNA adapted from Sambrook (2001). The restriction enzyme Bam HI was used for digestion to cut the plasmid DNA at a site that does not separate the T7 promoter contained in the pCRII-TOPO plasmid from the PCR insert. Plasmid DNA was purified by extractions using equal volumes of phenol/chloroform:isoamyl alcohol followed by 24:1 chloroform:isoamyl alcohol, and then precipitated with 3 M sodium acetate and cold ethanol. The product of the linearization was analyzed by agarose gel electrophoresis to ensure that a significant amount of circular plasmid DNA did not remain. Purified linearized DNA was resuspended in 1X TE and stored at 4°C.

Linearized DNA was in vitro transcribed from an adapted protocol for probe synthesis described in Sive et al. (2000) using a T7 RNA polymerase (Promega) and un-labeled rNTPs. Following the RNA synthesis reaction, samples were treated with 1 µl of RQ1 DNaseI I (Promega) at a concentration of 1 U/µl to remove residual DNA template. Probe integrity was assessed by 1.2% agarose gel electrophoresis. If a single band of the predicted molecular size of the RNA transcript was detected on the gel, purification of the RNA standard using the column based RNeasy Min-Elute Cleanup kit (Qiagen) was used to remove unincorporated nucleotides following the manufacturer's protocol.

Following RNA elution, RNA standard integrity and yield was again assessed by agarose gel electrophoresis. The RNA eluent was diluted 1:10 in nuclease-free H_2O and stored at -80°C.

Quantification and dilution of cRNA standards was performed following the protocol outlined by Fey et al. (2004). Briefly, cRNA concentrations were quantified spectrophotometically using a NanoDrop spectrometer after heating for 5 minutes at 60°C. A dilution series was created in a range of 0.001 fg to 1 ng in nuclease-free H_2O.

One-Step Real-Time PCR

Real-time PCR analysis was performed on DNaseI I treated experimental samples and cRNA standards in 50 μl singleplex reactions using the iScript One-Step RT-PCR kit for probes (Bio-Rad) in a Bio-Rad iCycler according to the manufacturer's instructions under the following conditions. Each forward and reverse primer for NIS and β-actin (See Table 2) was added at a 500 nM final concentration. TaqMan probes designed with a 6FAM fluorophore and TAMRA quencher (See Table 2) were added at 200 nM final concentration, and 500 ng of DNaseI-treated total RNA was used for each experimental sample reaction. The reaction protocol was performed according to the manufacturer's instructions beginning with cDNA synthesis for 10 minutes at 50°C followed by a reverse transcriptase inactivation for 5 minutes at 95°C. PCR cycling and detection consisted of 40 cycles of 15 seconds at 95°C and a data collection step of 30 seconds at 55.5 °C.

Experimental samples were comprised of tissues collected from imaged mice to quantitated NIS mRNA. Palpable tumors and portions of these tumors which demonstrated radioiodide uptake were compared with tumors containing regions of no radioiodide uptake activity. MMTV-infected mammary glands which had not developed palpable tumors were also examined. To compare these MMTV-infected mice with uninfected normal mice, mammary glands from nulliparous, multiparous, and lactating C57BL/6J mice were used. Thyroid was used as a positive control for NIS mRNA expression, and liver was used as a negative control. Each reaction was performed in duplicate. A parallel NIS and β-actin cRNA dilution series in a range of 0.001 fg to 1 ng was run to produce a standard curve for quantification of experimental mRNA transcripts.

Data Analysis

Real-time PCR results were analyzed using the critical threshold (Ct) value converted to mRNA transcript copy number using a cRNA standard curve. Ct values were determined by the Bio-Rad software, which designates the point at which the detection system reads a fluorescent signal associated with an exponential amplification of PCR product. Quantification of mRNA transcripts was determined using a combination of the methods described by Fronhoffs et al. (2002) and Fey et al. (2004). Briefly, a standard curve was created by plotting Ct values against the log of ng of cRNA standards for each gene. Unknown samples of NIS and β-actin were quantified using experimentally determined Ct values inserted to the equation of the line for each gene's standard curve. The conversion to mass units derived from the standard curve was performed by using the equation of the line of the linear regression analysis from each standard curve (Figures 1A and 1B). Using the calculated mass units of sample transcript, we then calculated mRNA starting copy number using the following formula adapted from Lee, et al. (2008).

$$\text{RNA copy number} = \frac{\text{mass of sample transcript (ng) x 6.022 x 10^23 (copies/mol)}}{\text{transcript length (bases/copy) x MW ribonucleotide (ng/mol)}}$$

The approximate molecular weight of a ribonucleotide within a region of single stranded RNA, $3.205\text{x}10^{11}$ (ng mol^{-1} bases^{-1}), was used for calculations (Applied Biosystems). The exact MW of each transcript was calculated, but was not found to be significantly different than the approximation used above. The transcript lengths for NIS and β-actin, including regions of plasmid DNA between the T7 promoter and BAM HI restriction enzyme cut site in addition to PCR inserts, were 243 and 218 nucleotides, respectively. Finally, a ratio of NIS copy number to β-actin mRNA copy number was calculated, using β-actin as an internal control for mRNA levels. The efficiency of each real-time experiment was determined using the slope of the standard curve with the following equation:

$$\text{Efficiency} = 10^{-1/\text{slope}} - 1,$$

with the slope determined from the equation of the linear regression curve of the dilutions of cRNA standard (Figures 1A and 1B).

To examine the relationship between radioiodide uptake and mRNA abundance, the ratio of NIS: β-actin was compared to the intensity and pattern of pixels within each ROI demonstrating radioiodide uptake. The abundance of NIS mRNA was correlated with one of two patterns of iodide uptake defined by our group in ROI analysis. The center-to-edge pattern describes radioiodide accumulation originating from a single location and spreading from this single starting point. Tumors exhibiting a multi-spot pattern demonstrated more than one region of initial radioiodide uptake.

TABLE 1: Primers used for Non-quantitative RT-PCR

Gene	NCBI Accession #	Sequence	Tm (°C)	GC%	Amplicon Size (bp)	Ref.
NIS	NM_053248	**F** 5’-CTGTACCCGCCTGGAGAG– 3’	57.3	66.6	201	Primer3
		R 5’-CCAGAGCCCCGTAGTAGAGA– 3’	57.6	60.0		
GAPDH	NM_008084	**F** 5’-AACTTTGGCATTGTGGAAGG– 3’	53.8	45.0	132	Primer3
		R 5’-GGATGCAGGGATGATGTTCT– 3’	54.7	50.0		
β-Actin	NM_007393	**F** 5’-AACACCCCAGCCATGTACGTAG– 3’	59.1	54.5	550	Perron,, 2001
		R 5’-GTGTTGGCATAGAGGTCTTTACGG– 3’	57.5	50.0		
		R 5’-ATAGATCATGGGCGGTTCAG– 3’	54.4	50.0		

TABLE 2: Primers and Probes used for TaqMan qRT-PCR

Gene	NCBI Accession #	Sequence	Tm (°C)	GC%	Beacon Rating	Amplicon Size (bp)
NIS	NM_053248	**F-** 5’- GCTCTCATTCATCTATGGCTCAAC-3’	58.5	45.8	78.3	130
		R- 5’-GGTGAAAGCGCCAAGGAGAG -3’	59.3	60.0	59.6	
		Probe- 5’-6FAM- TGTGGCTGCTCTGTCCTCGCTGCT-TAMRA -3’	69.2	62.5	87.8	
β-actin	NM_007393	**F-** 5’-TGTTTTGTTTTGGCGCTTTTGAC -3’	58.9	39.1	82.4	105
		R- 5’ -TCAGCCACATTTGTAGAACTTTGG -3’	58.7	41.7	57.9	
		Probe- 5’-6FAM- TGCTCCAACCAACTGCTGTCGCCT-TAMRA -3’	67.9	58.3	73.3	

RESULTS

cRNA Standard Curves

To determine the copy number of both NIS and β-actin transcripts in real-time RT-PCR analysis, we established standard curves using cRNA generated by in vitro transcription which was serially diluted in nuclease-free H_2O. cRNA standards were serially diluted in a range from 1 ng to 0.001 fg for each gene. Standard curves were generated for NIS and β-actin by plotting the Ct value versus log ng of cRNA standard (Figures 1A and 1B). A strong linear relationship was observed with a correlation coefficient of $r^2>0.99$. The efficiency of real-time amplification was also determined for of each cRNA curve. This efficiency calculation expresses the percentage to which each DNA template replicates itself per PCR cycle. Using the slope determined by the linear regression of the standard curve, the efficiency of amplification was 112% and 110% for NIS and β-actin, respectively. These values are at the upper range of acceptable limits for efficiency (Applied Biosystems).

MMTV- NIS mRNA Expression Controls: Thyroid and Liver

Confirmation of Primer Specificity and Sequence Analysis

In order to ensure that TaqMan primers for NIS and β-actin were specific for our genes of interest we performed non-quantitative RT-PCR to measure amplicon length, ensure the amplification of a single product, and verify the nucleotide sequence of each amplicon. Non-quantitative RT-PCR was performed using RNA from the thyroid of an MMTV mouse (mouse 240). Following RT-PCR, products were separated on 1.2% agarose gels. Products appeared at the expected molecular sizes; 130 base pairs and 105 base pairs for NIS and β-actin, respectively, without the presence of extraneous bands (Figure 2). Following cloning into a pCRII-TOPO vector, sequence analysis of the NIS and β-actin clones showed 100% identity with published sequences of each gene.

mRNA Quantification for Positive and Negative NIS Controls

The review by Dohan et al. (2003a) documents NIS mRNA expression in thyroid tissue, and no expression of NIS in liver tissue samples. Using these findings, we used thyroid as a positive tissue control and liver as a negative tissue control for NIS mRNA expression. We measured NIS and β-actin mRNA expression in thyroid and liver in an MMTV mouse (mouse 240). High levels of radioiodide uptake compared to background were recorded in the thyroid using gamma camera imaging (Figure 3A). Conversion of mean Ct values of three real-time RT-PCR replicates to mRNA transcript numbers revealed that the MMTV (mouse 240) thyroid contained $1.01\text{x}10^4$ NIS transcripts, compared with $3.62\ \text{x}10^6$ β-actin transcripts per 500 ng of total RNA. Liver mRNA was subjected to real-time RT-PCR and amplification did not cross the critical threshold following 40 PCR cycles, indicating little to no NIS expression (Figure 3A). β-actin transcript number in liver mRNA was calculated to be $1.38\ \text{x}10^7$ per 500 ng of total RNA. The NIS:β-actin ratio of thyroid and liver reveals that, when controlled for mRNA expression with an internal control gene, thyroid serves as a positive control for NIS mRNA expression while liver is a suitable negative control (Figure 3B).

MMTV-induced Mammary Tumors

In order to determine the level of NIS mRNA in mouse mammary tumors, we performed real-time RT-PCR on whole tumors or pieces of tumors (Table 3). We then compared the ratio of NIS mRNA to β-actin mRNA with the radioiodide uptake as revealed by gamma camera imaging. Below we present data from each of the analyzed tumors (Table 4). All data are presented as the NIS:β-actin ratio alongside a gamma camera image of the mouse.

Mouse 168: KI Blocked Mammary Tumor

The right thoracic mammary tumor of the MMTV-infected mammary tumor, which had been blocked with potassium iodide, was examined using real-time RT-PCR. KI blocking has the effect of reducing thyroid gland radioiodide uptake and preventing possible thyroid cell damage. It is not shown to affect tumor uptake in previous studies. The gamma camera image of this tumor indicates an increased radioiodide uptake above background throughout the area of the tumor, with a region of higher intensity in the center of the tumor (Figure 4). NIS and β-actin mRNA transcript numbers in this sample were calculated from the mean Ct value of one duplicate real-time reaction for each gene. The level of NIS transcripts was calculated to be 2.59×10^3, while the level of β-actin was calculated at 1.19×10^8 copies, each per 500 ng of total RNA.

Mouse 209: Mammary Tumor Cut into Four Pieces

The left thoracic mammary tumor of (mouse 209) was cut into four pieces and used for real-time RT-PCR. The exact position of each piece in relation to the gamma camera image was not documented in these tumors, reflecting a change in protocol between the time of tumor imaging and real-time processing in this instance. The gamma camera image of this tumor shows an increase in radioiodide uptake above background, with the anterior region of the tumor producing the highest level of uptake (Figure 5A). The ROI data confirms that the region at the anterior portion of the tumor shows an increase in radioiodide uptake compared with the other regions of the tumor (Figure 5B). ROI analysis identified this tumor as a center-to-edge pattern, which we have found to correlate with younger, still developing tumors. The mRNA transcript levels of NIS and β-actin cannot be correlated with the gamma camera image in this case, but differences in mRNA levels were documented between pieces of the tumor. Tumor morphology was documented prior to RNA extraction, and found each piece to be dense, white, tumor tissue. Piece 1 expressed 2.59×10^3 copies of NIS and 8.22×10^7 copies of β-actin per 500 ng of total RNA. Piece 2 expressed 4.22×10^3 copies of NIS and 2.15×10^6 copies of β-actin per 500 ng of total RNA. The third tumor piece was found to express 2.28×10^4 NIS transcripts and 8.85×10^7 β-actin transcripts per 500 ng of total RNA. Piece 4 expressed 9.99×10^3 copies of NIS and 5.26×10^7 copies of β-actin per 500 ng of total RNA. The comparison of NIS:β-actin ratio between the tumor pieces indicates that tumor piece two expressed significantly more mRNA than the other three tumor pieces when corrected for total mRNA expression (Figure 5C).

Mouse 229: Three Mammary Tumors Each Cut into Two Pieces

MMTV-infected (mouse 229) developed tumors in the right thoracic, right inguinal, and left abdominal mammary glands. Each tumor was excised and cut into two pieces, however, because these tumors were excised and frozen prior to the design of this experiment, the exact position of the cut in relation to the gamma camera image was not documented.

The right thoracic tumor was the largest and showed the highest quantity of radioiodide uptake among the three tumors (Figure 6A). The pattern of radioiodide uptake has not been examined using ROI analysis, but appears to be in the center-to-edge category. Both pieces of this tumor showed a dense, white morphology. Upon mRNA quantification with real-time PCR, this pieces A and B of this tumor expressed 3.24×10^3 and 2.49×10^3 NIS transcripts while expressing 8.85×10^7 and 7.08×10^7 β-actin transcripts per 500 ng of total RNA, respectively. When comparing NIS:β-actin ratio, both pieces A and B of the right thoracic tumor expressed more NIS mRNA than pieces of the two other tumors (Figure 6B).

The right inguinal tumor showed significant radioiodide uptake though not as high as the right thoracic tumor (Figure 6A). The pattern of radioiodide uptake was not examined with ROI analysis, but again appeared to have a center-to-edge character. The morphology of the tumor was dense and white. When examined with real-time PCR, piece A of the tumor expressed 1.71×10^3 NIS transcripts and 7.08×10^7 β-actin transcripts per 500 ng of total RNA. Tumor piece B expressed 7.50×10^2 NIS transcripts and 7.08×10^7 β-actin transcripts per 500 ng of total RNA.

The left abdominal tumor demonstrated a large decrease in radioiodide uptake from the other two tumors on this animal (Figure 6A). However, radioiodide accumulation did occur. The morphology of this tumor included regions of necrosis, but still consisted largely of dense, white tissue. mRNA quantification with real-time PCR showed that piece A expressed fewer NIS transcripts than piece B, 9.89×10^1

compared to 3.82×10^2 per 500 ng of total RNA. β-actin mRNA expression in piece A compared to piece B was also measured, with A expressing 8.85×10^7 transcripts and B expressing 1.19×10^8 per 500 ng of total RNA. The left abdominal tumor demonstrated the lowest NIS:β-actin ratio among the three tumors in (mouse 229) (Figure 6B).

Mouse 240: Mammary Tumor Cut into Five Pieces

The left inguinal tumor of (mouse 240) was separated into five pieces and corresponding designations were indicated on the gamma camera image and ROI analysis plot (Figures 7A and 7B). Through ROI analysis, this tumor was identified as having a multi-spot uptake pattern. We have found this pattern to correlate with older tumors. Within the tumor, Piece 1 had the most radioiodide uptake, while Piece 5 displayed the lowest amount of radioiodide uptake on gamma camera images. The morphology of pieces 2-5 appeared white and dense. However, tumor piece 1 had large regions of necrosis and largely bloody prior to mRNA extraction. Each individual piece of the tumor was then used in real-time RT-PCR where NIS and β-actin copy numbers were determined. NIS and β-actin transcript numbers were 8.09×10^2 and 1.38×10^8 per 500 ng of total RNA, respectively in Piece 1. In Piece 2, NIS mRNA expressed 2.02×10^2 copies, while expressing 5.26×10^7 copies of β-actin mRNA per 500 ng of total RNA. Piece 3 expressed 1.32×10^3 copies of NIS mRNA and 9.54×10^7 copies of β-actin mRNA per 500 ng of total RNA. In piece 4, it was calculated that the tumor expressed 6.89 copies of NIS and 7.08×10^7 copies of β-actin mRNA per 500 ng of total RNA. These values resulted after four replicates of both NIS and β-actin real-time runs, with two of the four providing quantities of NIS mRNA that did not cross the critical threshold before cycle

40. Piece 5 of this tumor expressed 2.40×10^3 copies of NIS mRNA and 7.63×10^7 copies of β-actin mRNA per 500 ng of total RNA, the highest amount within this tumor. Tumor piece 5 showed over a two-fold increase in NIS mRNA expression compared to any of the other pieces within this tumor when normalized to β-actin expression, while piece 3 exhibited a two-fold increase over both pieces 1 and 2 (Figure 7C).

Mouse 258: Mammary Tumor Piece

The right thoracic mammary tumor of (mouse 258) was used in real-time RT-PCR. The piece of the tumor used in these experiments was the half toward the center of the animal. This region appeared white and dense, while the outer region appeared more bloody and necrotic. The gamma camera image shows increased radioiodide uptake above background throughout the tumor (Figure 8B). It also shows a higher intensity of radioiodide signal in the inner region of the tumor which was used in these real-time experiments. The NIS and β-actin copy numbers were calculated from the mean Ct of three replicate real-time reactions for each gene. Transcript numbers of NIS and β-actin mRNA were calculated as 9.61×10^2 and 7.08×10^7 per 500 ng of total RNA, respectively.

MMTV- Non-Palpable Tumor Mammary Glands

We investigated NIS expression in mammary glands of MMTV mice lacking palpable tumors as a reference for any changes in expression demonstrated by tumor tissues. In addition, we aimed to measure increases in NIS expression at the earliest stage of tumor development. In order to determine the level of mRNA expressed in mammary glands with non-palpable tumors of MMTV-infected mice, we performed real-time RT-

PCR and compared NIS:β-actin transcript ratios with the amount of radioiodide uptake in gamma camera images.

Mouse 256 Non- Tumor Mammary Gland

The left inguinal mammary gland of (mouse 256) was excised and NIS mRNA transcript levels were examined using real-time RT-PCR. The gamma camera image of this mammary gland displays radioiodide uptake slightly above the background level (Figure 8A). When mean Ct values of duplicate RT-PCR runs were converted into mRNA transcript number, NIS was expressed at 2.49×10^3 mRNA transcripts, while β-actin was expressed at a level of 4.06×10^7 transcripts per 500 ng of total RNA. When NIS:β-actin transcript ratios were compared with other non-tumor mammary glands in MMTV-mice, (mouse 256) showed a normalized NIS expression ratio in between that of the small tumor in (mouse 258) and the non-tumor mammary gland showing no radioiodide uptake in (mouse 262) (Figure 8D).

Mouse 258 Non-Palpable Small Tumor

The left inguinal mammary gland of (mouse 258) was examined by comparing NIS mRNA transcript ratio with the internal control β-actin with the amount of radioiodide uptake above background in the gamma camera image. The level of radioiodide uptake in the left inguinal mammary gland of the mouse is significantly higher than background (Figure 8B). Real-time RT-PCR analysis of four replicate samples showed that NIS transcripts were expressed at a level of 1.01×10^3 and β-actin transcripts were expressed at a level of 8.05×10^6 per 500 ng of total RNA. The NIS:β-actin transcript ratio in the small tumor in (mouse 258) showed much greater normalized NIS mRNA expression than the large, developed tumor in the right thoracic region of same animal (Figure 8E).

Mouse 262 Non-Tumor Mammary Gland

The left inguinal mammary gland of (mouse 262) was observed for the amount of radioiodide accumulation above background compared with the amount of NIS mRNA. The gamma camera image does not appear to have radioiodide uptake above the level of background in the region of the left inguinal mammary gland (Figure 8C). In a duplicate real-time reaction, the levels of NIS mRNA and β-actin were calculated to be 1.27×10^3 mRNA transcripts and 3.49×10^7 mRNA transcripts per 500 ng of total RNA, respectively.

C57- Lactating, Multiparous and Nulliparous Mammary Glands

NIS mRNA Expression in C57 Mammary Glands Shown by Non-quantitative RT-PCR

Non-quantitative RT-PCR was performed on mammary glands of lactating, previously pregnant, and nulliparous C57 mice to determine if NIS mRNA was present in each tissue as documented by current literature (Dohan, 2003a). RT-PCR was performed with primers for NIS and β-actin using lactating mice 251 and 253, previously pregnant mice 250 and 254, and nulliparous mice 249 and 255. PCR products were separated on 1.2% agarose gels, and stained with ethidium bromide to visualize bands. Bands of the expected molecular size (201 base pairs) were observed in all of the above tissues (Figure 9). No RT negative controls were performed for each primer set in each reaction.

mRNA Quantification in Lactating Mammary Glands in C57 Mice

To determine the differences in NIS mRNA expression between the three categories of C57 mammary glands, real-time RT-PCR was performed on samples from each set. Lactating mammary glands from (mice 251 and 253) were examined using real-time RT-PCR. The right axillary gland from (mouse 251) and the left axillary gland from (mouse 253) were used in experiments. Both glands showed high levels of radioiodide uptake by gamma camera imaging (Figures 10A and 10B). When analyzed with real-time RT-PCR, (mouse 251) was found to have 5.48×10^3 NIS transcripts and 1.80×10^7 β-actin transcripts per 500 ng of total RNA when derived from mean Ct values of six replicates. In (mouse 253), duplicates real-time reactions produced 1.63×10^4 NIS transcripts and 8.51×10^6 β-actin transcripts per 500 ng of total RNA. The lactating mammary glands each show increased NIS mRNA expression compared to previously pregnant and nulliparous animals (Figure 10E). However, (mouse 251) expresses much less NIS mRNA than (mouse 253).

mRNA Quantification in Mammary Glands of Previously Pregnant C57 Mice

To measure the quantity of NIS mRNA transcripts in previously pregnant, multiparous C57 mice, real-time PCR was performed on the right inguinal mammary gland of (mouse 250). In the gamma camera image of this animal, radioiodide uptake was not above background levels (Figure 10C). When transcript copy number was derived following real-time PCR, 3.77×10^3 NIS mRNA transcripts and 2.90×10^7 β-actin transcripts per 500 ng of total RNA were recorded.

mRNA Quantification in Mammary Glands of Nulliparous C57 Mice

To determine the level of NIS mRNA expression in mammary glands of nulliparous (virgin) C57 mice, we performed real-time RT-PCR on the right axillary mammary gland of (mouse 255). The gamma camera image of this mouse does not demonstrate a level of radioiodide uptake above background in the region of the right axillary mammary gland (Figure 10D). When transcript numbers of NIS and β-actin were calculated, NIS mRNA transcripts were detected at a level of 3.12×10^3, while β-actin transcripts were present at levels of 1.10×10^7 per 500 ng of total RNA.

Table 3. Raw data from real-time RT-PCR. Input total RNA for each sample was 500 ng. Letters designate when a new DNaseI treatment is performed on original RNA extraction. Numbers following a letter or a hyphen designate the number of freeze-thaw cycles each DNased RNA has undergone. No letter or number indicates freshly DNased RNA that has not been frozen.

Mouse# - Tissue	**NIS Ct 1**	**NIS Ct 2**	**NIS Ct 3**	**NIS Ct 4**	**NIS Ct 5**	**NIS Ct 6**	**NIS Mean Ct**	**NIS SD**	**NIS %CV**	**Actin Ct 1**	**Actin Ct 2**	**Actin Ct 3**	**Actin Ct 4**	**Actin Ct 5**	**Actin Mean Ct**	**Actin SD**	**Actin %CV**
168 KI Blocked MMTV Tumor	27.1	29.8					28.45	1.35	4.75	13.2	12.7				12.95	0.25	1.93
209-1 MMTV Tumor Piece	28.1	28.8					28.45	0.35	1.23	13.7	14				13.85	0.15	1.08
209-2 MMTV Tumor Piece	28.7	28.7	27.1a	27.5a	27.0a1		27.8	0.75	2.70	18.6	18.6	13.4a	13.1a	14.1a1	15.56	2.5	16.07
209-3 MMTV Tumor Piece	25.6	25.5					25.55	0.05	0.196	13.6	13.6				13.6	0	0
209-4 MMTV Tumor Piece	26.7	26.6					26.65	0.05	0.188	14.3	14				14.15	0.15	1.06
229-RT-A Tumor Piece	27.9						27.9	N/A	N/A	13.6					13.6	N/A	N/A
229-RT-B Tumor Piece	28.5						28.5	N/A	N/A	13.9					13.9	N/A	N/A
229-RI-A Tumor Piece	29						29	N/A	N/A	13.9					13.9	N/A	N/A
229-RI-B Tumor Piece	30.1						30.1	N/A	N/A	13.9					13.9	N/A	N/A
229-LA-ATumor Piece	32.8						32.8	N/A	N/A	13.6					13.6	N/A	N/A
229-LA-B Tumor Piece	31						31	N/A	N/A	13.2					13.2	N/A	N/A
240-1 MMTV Tumor Piece	N/A	30					30	N/A	N/A	13	13.1				13.05	0.05	0.383
240-2 MMTV Tumor Piece	34.4	29.3					31.85	2.55	8.01	14.3	14.1				14.2	0.1	0.704

240-3 MMTV Tumor Piece	29.9	28.8					29.35	0.55	1.87	13.5	13.3				13.4	0.1	0.746
240-4 MMTV Tumor Piece	N/A	N/A	37.6a	35.1a1			36.35	1.25	3.44	13.9	13.9	12.8a	14a1		13.65	0.49	3.59
240-5 MMTV Tumor Piece	28.3	28.8					28.55	0.25	0.876	13.8	13.8				13.8	0	0
258 MMTV Tumor Piece	29.6	29.3	30.4a				29.77	0.46	1.55	13.9	14.2	14.0-1			14.03	0.125	0.891
258 MMTV Small Tumor	33.7	28.6	28.4a	28.1a			29.7	2.3	7.74	19	19.1	14.6a	14.6a		16.825	2.225	13.22
256 MMTV Non Tumor Mammary Gland	28.2	28.8					28.5	0.3	1.05	14.7	14.6				14.65	0.05	0.341
262 MMTV Non Tumor Mammary Gland	30	28.8					29.4	0.6	2.04	14.7	15				14.85	0.15	1.01
251 C57 Lactating Mammary Gland	31.5	30.9	25.8a	26.2a1	25.2a2	25.1a2	27.45	2.68	9.76	16.4	16.4	15a	15.7a1	15.2a2	15.74	0.585	3.72
253 C57 Lactating Mammary Gland	25.9	26.1					26	0.1	0.385	17	16.5				16.75	0.25	1.49
250 C57 Multiparous Mammary Gland	27.9	28					27.95	0.05	0.179	15.1					15.1	N/A	N/A
255 C57 Nulliparous Mammary Gland	28.2						28.2	N/A	N/A	16.4					16.4	N/A	N/A
240- MMTV Thyroid	26.7	26.3-1	26.9-1				26.63	0.25	0.939	17.9					17.9	N/A	N/A
240- MMTV Liver	N/A						N/A	N/A	N/A	16.1					16.1	N/A	N/A

Table 4. NIS copy number, β-actin copy number, and NIS:β-actin ratio.

Mouse # and Tissue	**NIS transcripts**	**β-actin transcripts**	**NIS:β-actin Ratio**
168 KI Blocked MMTV Tumor	$4.90x10^{3}$	$2.26x10^{8}$	$2.17\ x10^{-5}$
209-1 MMTV Tumor Piece	$4.90x10^{3}$	$1.56x10^{8}$	$3.15\ x10^{-5}$
209-2 MMTV Tumor Piece	$7.99x10^{3}$	$4.07x10^{6}$	$1.96\ x10^{-3}$
209-3 MMTV Tumor Piece	$4.32x10^{4}$	$1.68x10^{8}$	$2.58\ x10^{-4}$
209-4 MMTV Tumor Piece	$1.89x10^{4}$	$9.97x10^{7}$	$1.90\ x10^{-4}$
229-RT-A Tumor Piece	$6.14x10^{3}$	$1.68x10^{8}$	$3.66\ x10^{-5}$
229-RT-B Tumor Piece	$4.72x10^{3}$	$1.34x10^{8}$	$3.52\ x10^{-5}$
229-RI-A Tumor Piece	$3.25x10^{3}$	$1.34x10^{8}$	$2.42\ x10^{-5}$
229-RI-B Tumor Piece	$1.42x10^{3}$	$1.34x10^{8}$	$1.06\ x10^{-5}$
229-LA-ATumor Piece	$1.87x10^{2}$	$1.68x10^{8}$	$1.12\ x10^{-6}$
229-LA-B Tumor Piece	$7.24x10^{2}$	$2.26x10^{8}$	$3.20\ x10^{-6}$
240-1 MMTV Tumor Piece	$1.53x10^{3}$	$2.62x10^{8}$	$5.85\ x10^{-6}$
240-2 MMTV Tumor Piece	$3.82x10^{2}$	$9.97x10^{7}$	$3.83\ x10^{-6}$
240-3 MMTV Tumor Piece	$2.50x10^{3}$	$1.81x10^{8}$	$1.38\ x10^{-5}$
240-4 MMTV Tumor Piece	$1.13x10^{1}$	$1.34x10^{8}$	$9.72\ x10^{-8}$
240-5 MMTV Tumor Piece	$4.55x10^{3}$	$1.45x10^{8}$	$3.15\ x10^{-5}$
258 MMTV Tumor Piece	$1.82x10^{3}$	$1.34x10^{8}$	$1.36\ x10^{-5}$
258 MMTV Small Tumor	$1.92x10^{3}$	$1.52x10^{7}$	$1.26\ x10^{-4}$
256 MMTV Non Tumor Mammary Gland	$4.72x10^{3}$	$7.69x10^{7}$	$6.15\ x10^{-5}$
262 MMTV Non Tumor Mammary Gland	$2.40x10^{3}$	$6.62x10^{7}$	$3.63\ x10^{-5}$
251 C57 Lactating Mammary Gland	$1.04x10^{4}$	$3.42x10^{7}$	$3.04\ x10^{-4}$
253 C57 Lactating Mammary Gland	$3.08x10^{4}$	$1.61x10^{7}$	$1.91\ x10^{-3}$
250 C57 Multiparous Mammary Gland	$7.14x10^{3}$	$5.50x10^{7}$	$1.30\ x10^{-4}$
255 C57 Nulliparous Mammary Gland	$5.92x10^{3}$	$2.09x10^{7}$	$2.83\ x10^{-4}$
240-MMTV Thyroid	$1.92x10^{4}$	$6.86\ x10^{6}$	$2.80\ x10^{-3}$
240-MMTV Liver	0	$2.61x10^{7}$	0

Figure 1. cRNA standard curves.

Standard curves were generated for (A) NIS and (B) β-actin. Ten-fold serial dilutions of cRNA standards were performed in nuclease free H2O, and five dilutions over the range of 1 ng to 0.1 fg were quantified using real-time RT-PCR (0.1 fg, 1 fg, 1 pg, 10 pg, 1 ng). A standard curve graph is made by plotting Ct value on the y-axis and the log of input amount (nanograms of cRNA) on the x-axis. The slope of the NIS cRNA standard curve (A) is -3.0681, the equation of the line is

$y = (-3.0681x + 9.4349)$, and the correlation coefficient is 0.9972. The slope of the β-actin cRNA standard curve (B) is -3.0964, the equation of the line is

$y = (-3.0964x + 8.303)$, and the correlation coefficient is 0.9989.

A

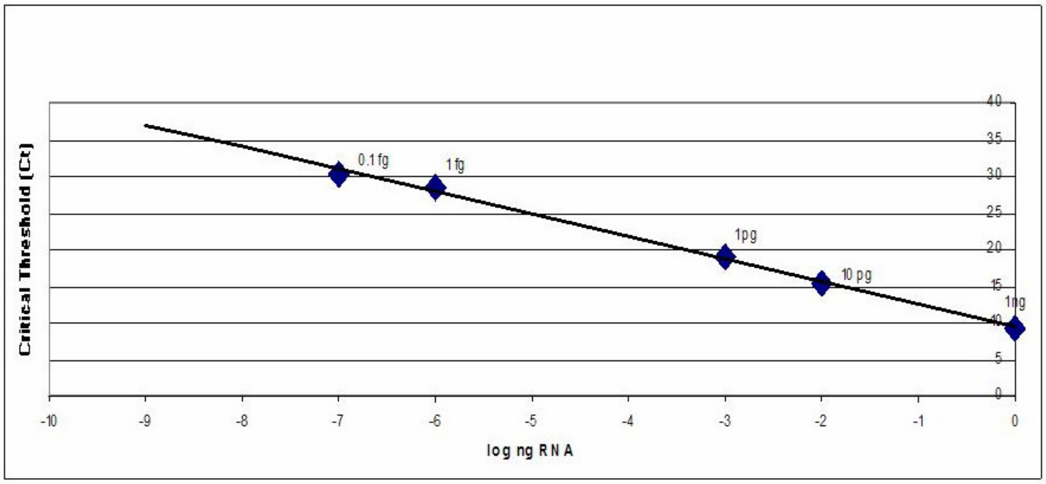
Critical Threshold (Ct)
40
35
30
25
20
15
10
5
0
0.1 fg
1 fg
1pg
10 pg
1ng
-10
-9
-8
-7
-6
-5
-4
-3
-2
-1
0
log ng RNA

B

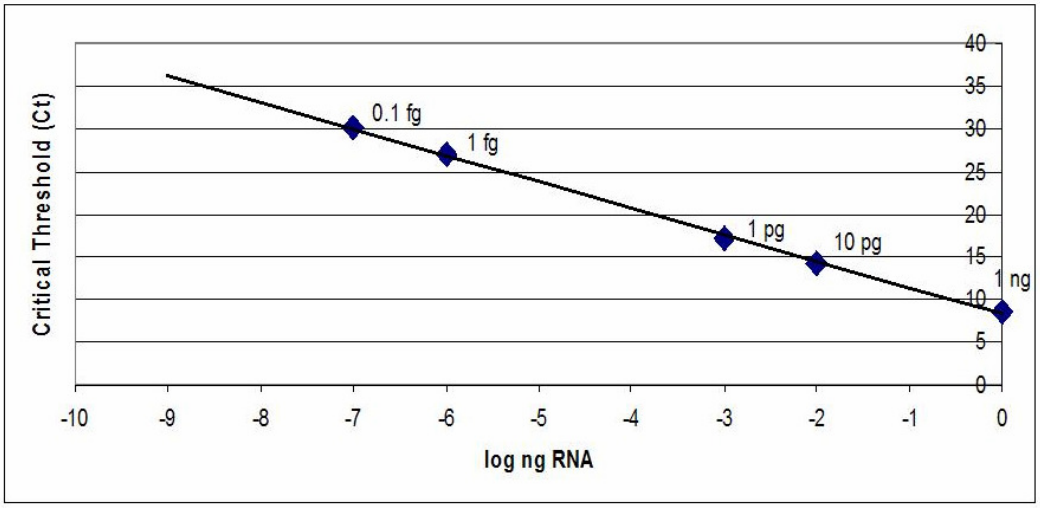
Critical Threshold (Ct)
40
35
30
25
20
15
10
5
0
0.1 fg
1 fg
1 pg
10 pg
1 ng
-10
-9
-8
-7
-6
-5
-4
-3
-2
-1
0
log ng RNA

Figure 2. Non-quantitative RT-PCR amplifying NIS and β-actin with TaqMan Primers.

RT-PCR was performed on thyroid RNA extracted from an MMTV-mouse (mouse 240) using TaqMan primers designed for real-time RT-PCR. NIS PCR product appeared as a single band at 130 base pairs (Lane 2) and β-actin PCR product appeared as a single band at 105 base pairs (Lane 4) as measured by a 1Kb+ ladder (Lane 1). No RT controls were performed for each gene (Lanes 3 and 5).

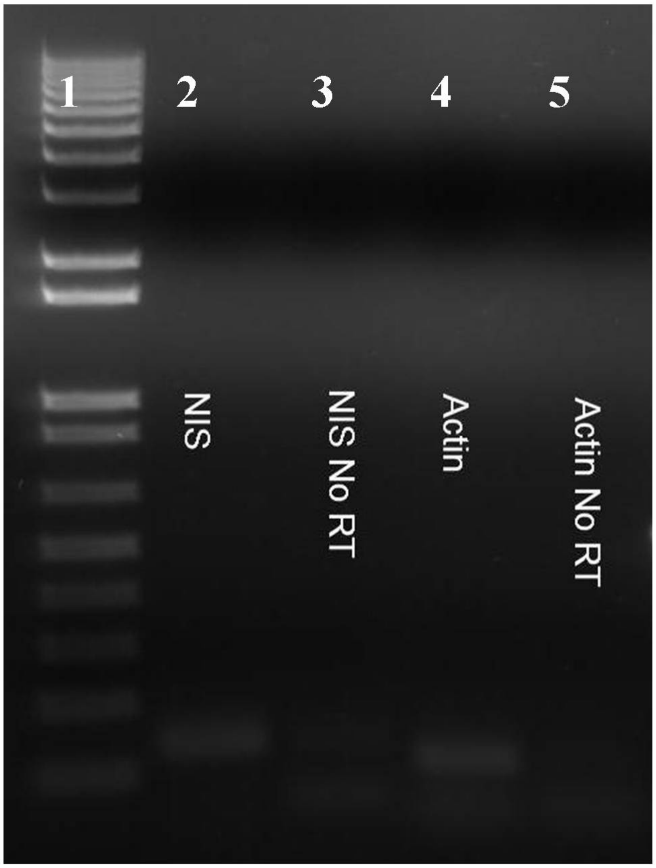
1
2
3
4
5
NIS
NIS No RT
Actin
Actin No RT

Figure 3. Positive and negative control tissues for NIS mRNA expression.

Thyroid gland and liver, designated by red box, of an MMTV mouse (mouse 240) were imaged with the gamma camera (A). Thyroid revealed high levels of radioiodide uptake, while liver did not accumulate radioiodide above background levels. Real-time PCR was performed using 500 ng of total RNA extracted from each tissue to record levels of NIS and β-actin mRNA. The mean Ct values for each gene were converted into transcript copy number. Data are presented as a ratio of NIS: β-actin transcript copy number (B). Thyroid expressed NIS mRNA, proving it to be a suitable positive control, while liver did not produce a signal for NIS following 40 real-time PCR cycles, exhibiting its suitability as a negative control.

A

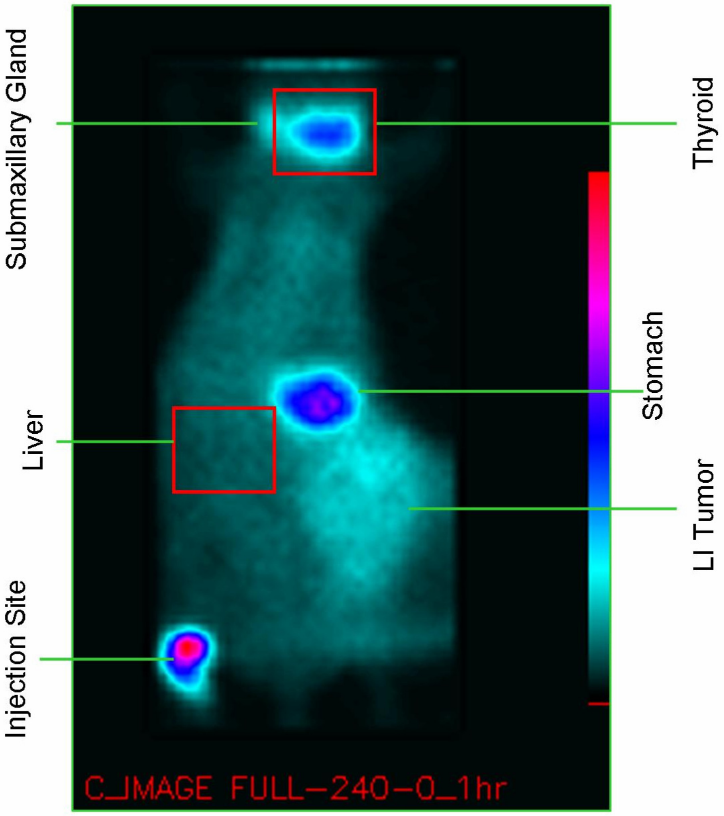
Submaxillary Gland
Thyroid
Stomach
Liver
LI Tumor
Injection Site
C_IMAGE FULL-240-0_1hr

B

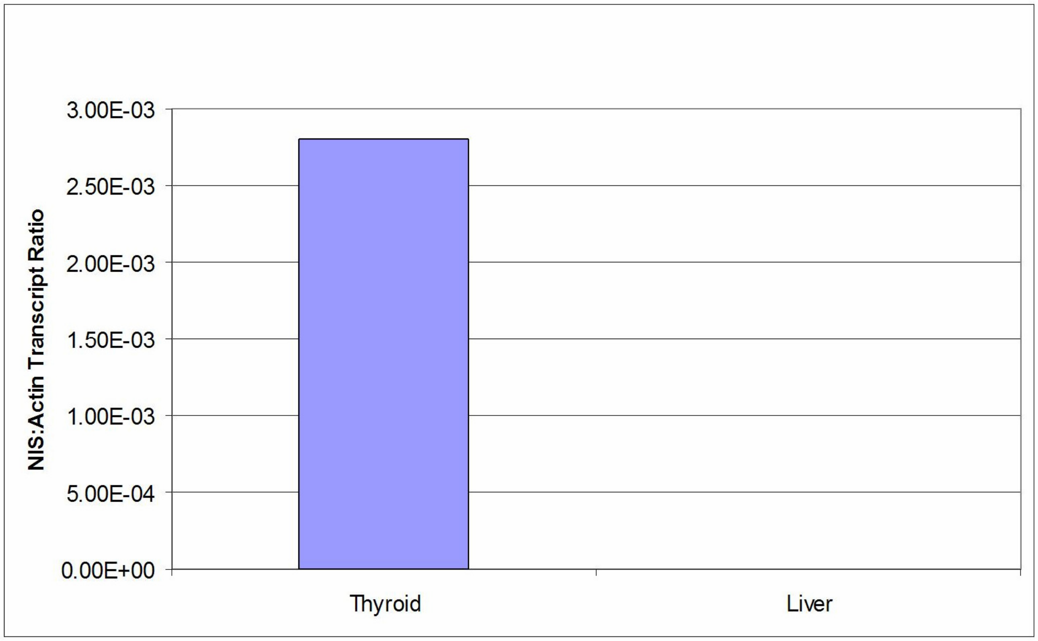
NIS:Actin Transcript Ratio
3.00E-03
2.50E-03
2.00E-03
1.50E-03
1.00E-03
5.00E-04
0.00E+00
Thyroid
Liver

Figure 4. MMTV-mouse (mouse 168) with potassium iodide blocking.

The gamma camera image of KI-blocked MMTV mouse (mouse 168) showed accumulation of radioiodide in right thoracic (RT) tumor, designated by a red box. KI blocking has the effect of reducing thyroid gland radioiodide uptake and preventing possible thyroid cell damage. It is not shown to affect tumor uptake in previous studies. Real-time RT-PCR was performed on this tumor to determine NIS and β-actin mRNA levels.

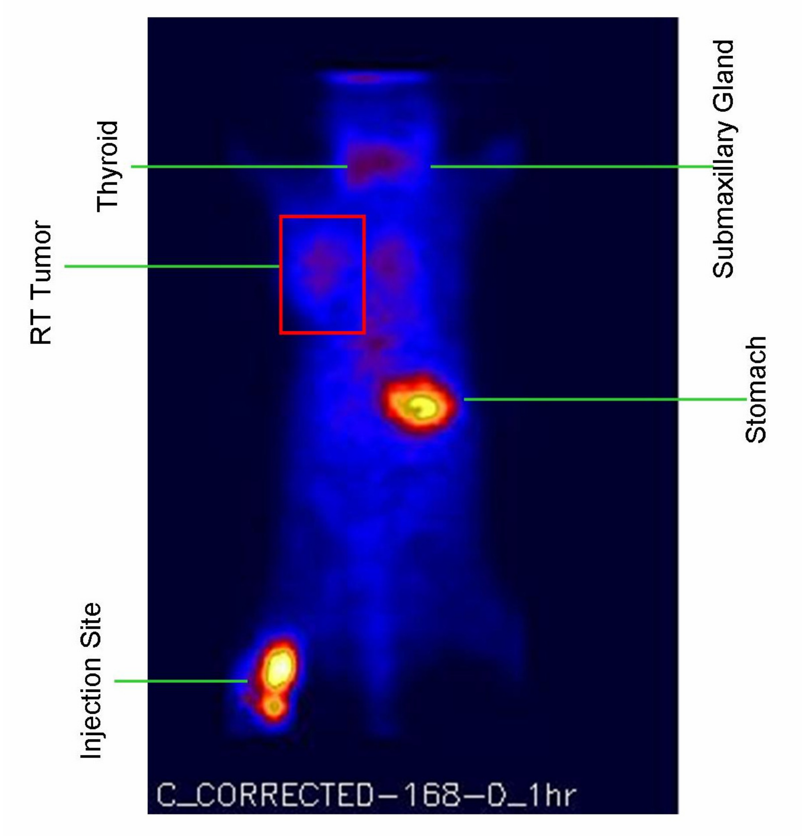
Thyroid
RT Tumor
Injection Site
Submaxillary Gland
Stomach
C_CORRECTED-168-D_1hr

Figure 5. Comparison of radioiodide uptake and NIS mRNA level in MMTV mouse (mouse 209) which has developed one mammary tumor.

MMTV-infected mouse (mouse 209) was imaged with the gamma camera and revealed radioiodide uptake in the left thoracic (LT) mammary tumor (A). The region of this tumor, marked by a red box, was investigated with ROI analysis (B), displaying a center-to-edge pattern of radioiodide uptake. The tumor was removed and separated into four sections (209-1, 209-2, 209-3, and 209-4). The orientation of these pieces in relation to the gamma camera image was not recorded. Real-time PCR was performed using 500 ng of total RNA extracted from each tumor piece to record levels of NIS and β-actin mRNA. The mean Ct values for each gene were converted into transcript copy number. Data are presented as a ratio of NIS: β-actin transcript copy number (C).

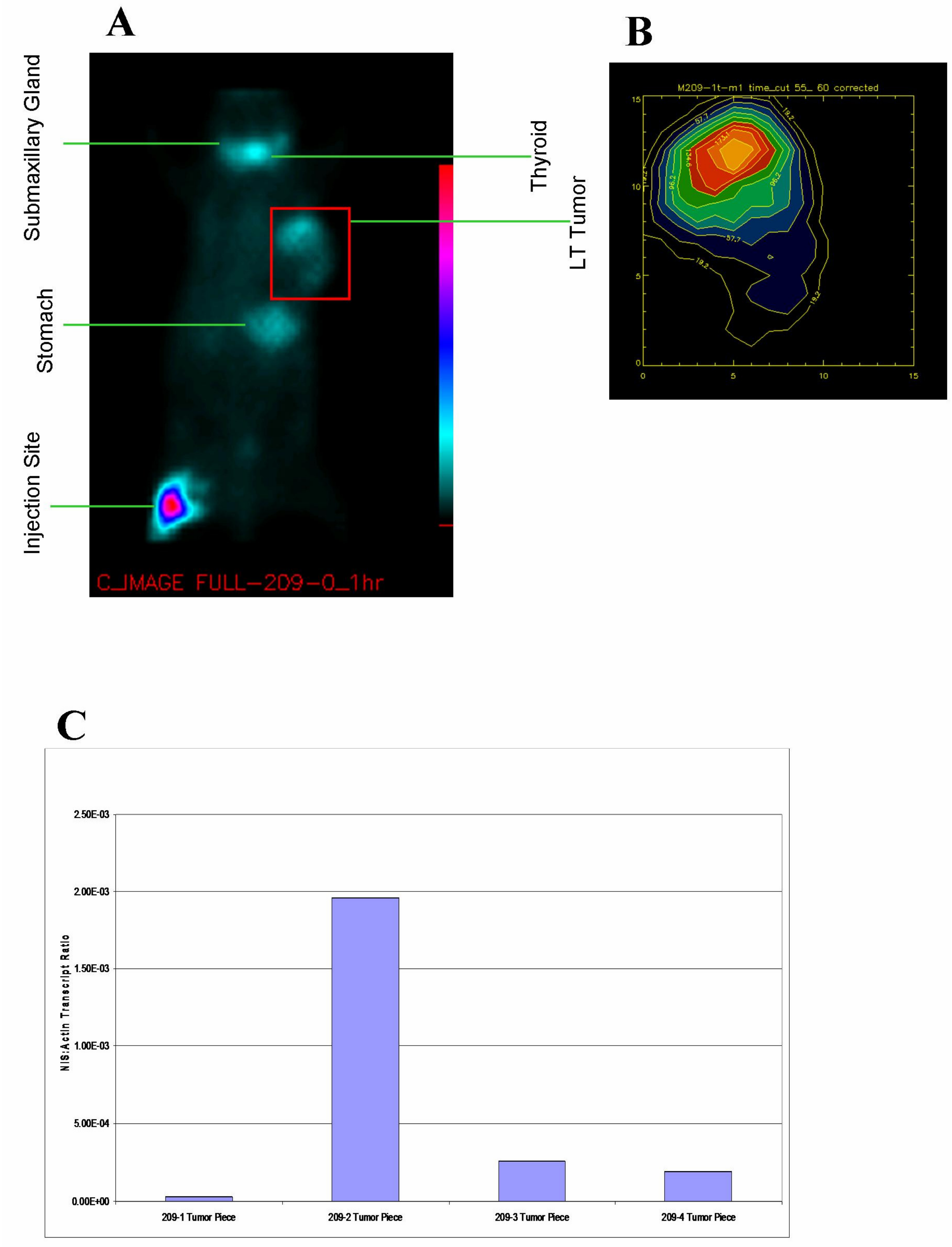
A
Submaxillary Gland
Stomach
Injection Site
Thyroid
LT Tumor
C_IMAGE FULL-209-0_1hr
B
M209-1t-m1 time_cut 55_ 60 corrected
15
10
5
0
0
5
10
15
19.2
57.7
96.2
134.6
173.1
C
NIS:Actin Transcript Ratio
2.50E-03
2.00E-03
1.50E-03
1.00E-03
5.00E-04
0.00E+00
209-1 Tumor Piece
209-2 Tumor Piece
209-3 Tumor Piece
209-4 Tumor Piece

Figure 6. Comparison of radioiodide uptake and NIS mRNA level in MMTV mouse (mouse 229) which has developed three mammary tumors.

MMTV-infected mouse (mouse 229) was imaged with the gamma camera and revealed radioiodide uptake in right thoracic (RT), right inguinal (RI), and left abdominal (LA) mammary tumor tumors(A). The RT tumor exhibited the most radioiodide uptake, while the RA tumor showed the least radioiodide uptake. Each tumor is marked with a red box encompassing the region of the tumor which was excised and examined with real-time RT-PCR. Following removal, each tissue was split into two pieces (A and B). The orientation of the tumor halves in relation to the gamma camera image was not recorded. Real-time PCR was performed using 500 ng of total RNA extracted from each tumor piece to record levels of NIS and β-actin mRNA. The mean Ct values for each gene were converted into transcript copy number. Data are presented as a ratio of NIS: β-actin transcript copy number (B). Increased mRNA level correlates with increased radioiodide uptake in the comparison of the three tumors, as the RT tumor contains the highest NIS:β-actin ratio in addition to the highest level of radioiodide accumulation within the tumor. The RI tumor has the second highest levels of NIS: β-actin ratio and radioiodide uptake. The LA tumor has the lowest levels of each.

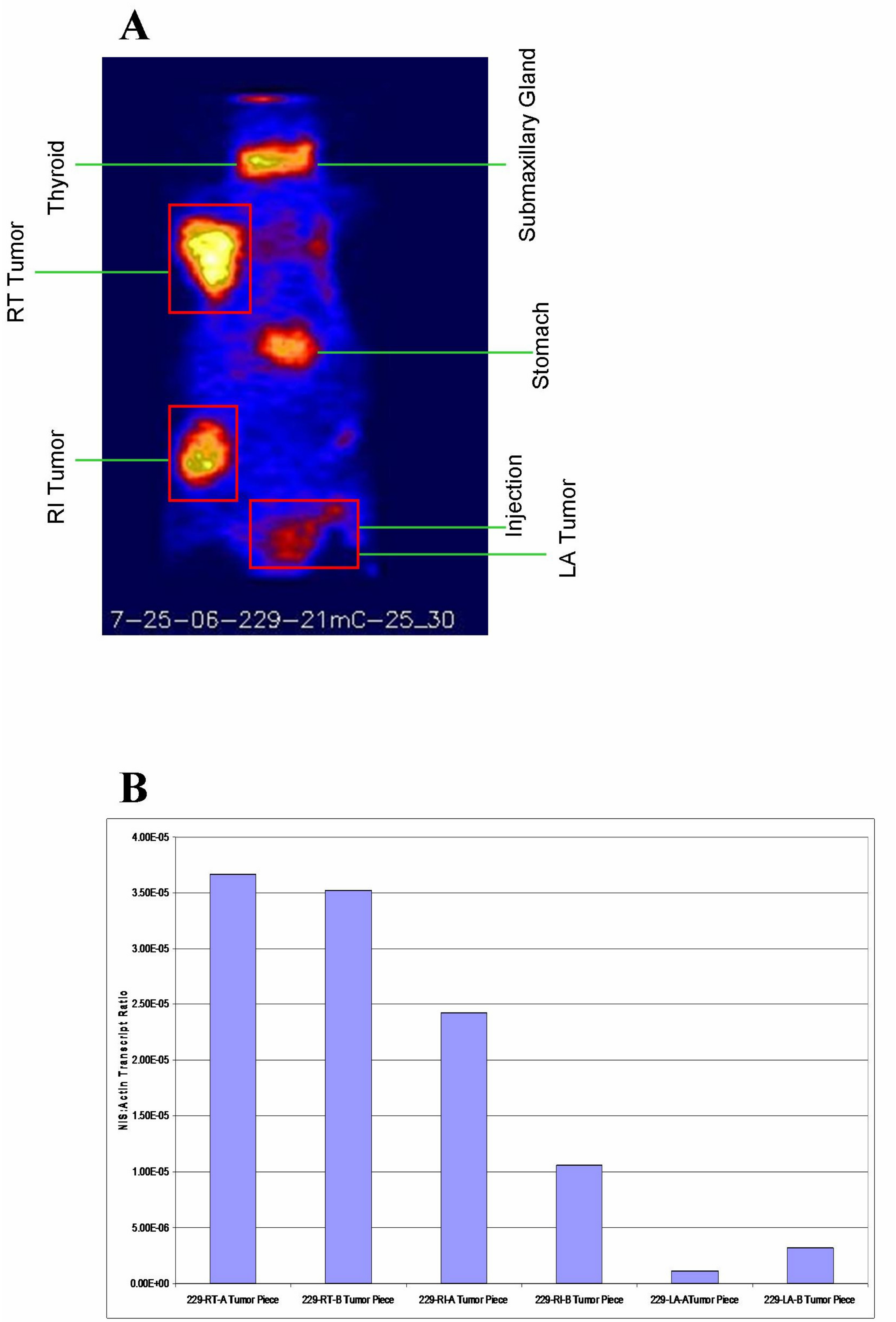
A
Thyroid
RT Tumor
RI Tumor
Submaxillary Gland
Stomach
Injection
LA Tumor
7-25-06-229-21mC-25_30
B
NIS:Actin Transcript Ratio
4.00E-05
3.50E-05
3.00E-05
2.50E-05
2.00E-05
1.50E-05
1.00E-05
5.00E-06
0.00E+00
229-RT-A Tumor Piece
229-RT-B Tumor Piece
229-RI-A Tumor Piece
229-RI-B Tumor Piece
229-LA-ATumor Piece
229-LA-B Tumor Piece

Figure 7. Comparison of radioiodide uptake and NIS mRNA level in MMTV mouse (mouse 240) which has developed one mammary tumor.

MMTV-infected mouse (mouse 240) was imaged with the gamma camera and revealed radioiodide uptake in a left inguinal (LI) mammary tumor (A). The region of this tumor, marked by a red box, was investigated with ROI analysis (B), displaying a multi-spot pattern of radioiodide uptake. The tumor was removed and separated into five sections (240-1, 240-2, 240-3, 240-4, and 240-5). The orientation of these pieces in relation to the gamma camera is presented in the ROI image (B). Real-time PCR was performed using 500 ng of total RNA extracted from each tumor piece to record levels of NIS and β-actin mRNA. The mean Ct values for each gene were converted into transcript copy number. Data are presented as a ratio of NIS: β-actin transcript copy number (C). The mRNA levels in the tumor pieces do not correlate with increased radioiodide uptake in the pieces of this tumor. Tumor piece 240-5 has the lowest amount of radioiodide uptake as seen in the ROI analysis (B), but contains the highest ratio of NIS:β-actin transcripts. Additionally, pieces 240-1 and 240-2 reveal the highest radioiodide uptake in ROI analysis; however they possess the lower ratios of NIS: β-actin transcripts than piece 240-5.

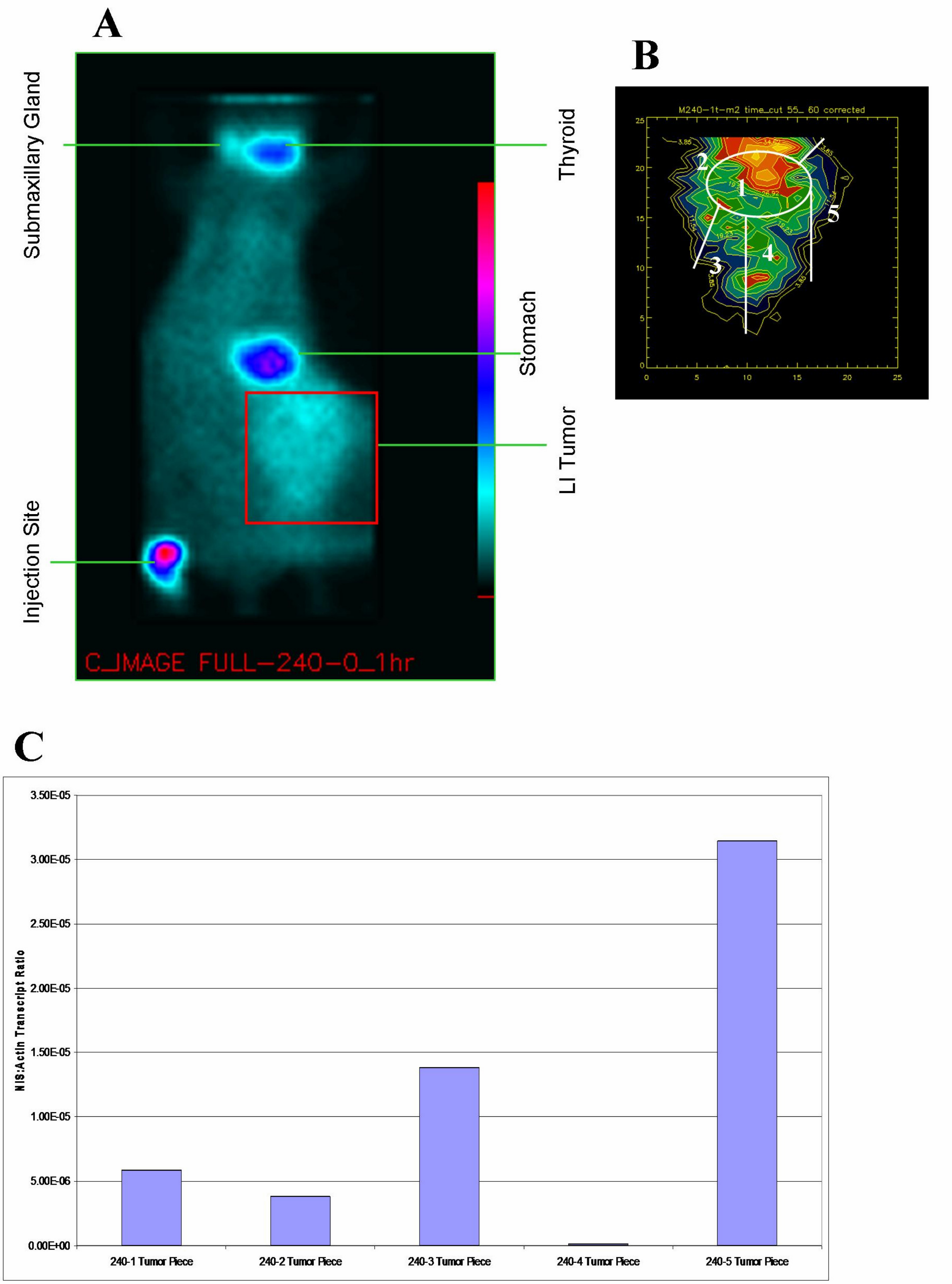
A
Submaxillary Gland
Thyroid
Stomach
LI Tumor
Injection Site
C_IMAGE FULL-240-0_1hr
B
M240-1t-m2 time_cut 55_ 60 corrected
1
2
3
4
5
3.85
34.62
26.92
19.23
11.54
0
5
10
15
20
25
C
NIS:Actin Transcript Ratio
3.50E-05
3.00E-05
2.50E-05
2.00E-05
1.50E-05
1.00E-05
5.00E-06
0.00E+00
240-1 Tumor Piece
240-2 Tumor Piece
240-3 Tumor Piece
240-4 Tumor Piece
240-5 Tumor Piece

Figure 8. Comparison of radioiodide uptake and NIS mRNA level in multiple MMTV mice (mouse 256, mouse 258, and mouse 262) in mammary glands with non-palpable tumors.

An MMTV-infected mouse (mouse 256) was imaged with the gamma camera and revealed radioiodide uptake in the right thoracic (RT) mammary tumor. Radioiodide uptake was increased above background levels in the left inguinal non-tumor mammary gland, designated by a red box (A). An MMTV-infected mouse (mouse 258) was imaged with the gamma camera and accumulated iodide in a right thoracic tumor as well as a mammary gland in the left inguinal region, each designated by a red box (B). An MMTV-infected mouse (mouse 262) developed a left thoracic tumor which accumulated radioiodide. We investigated the left-inguinal non-tumor mammary gland of this mouse, which did not accumulate radioiodide above background levels. Real-time PCR was performed using 500 ng of total RNA extracted from each mammary gland to record levels of NIS and β-actin mRNA. The mean Ct values for each gene were converted into transcript copy number. Data are presented as a ratio of NIS: β-actin transcript copy number (D). Amounts of radioiodide uptake and NIS: β-actin transcripts correlate between each of these non-tumor mammary glands. A comparison of NIS: β-actin transcripts between the large tumor and the non-palpable tumor of mouse 258 was conducted (E). This graph shows a significant increase in NIS: β-actin ratio in a developing tumor compared with an older tumor which has already accumulated iodide.

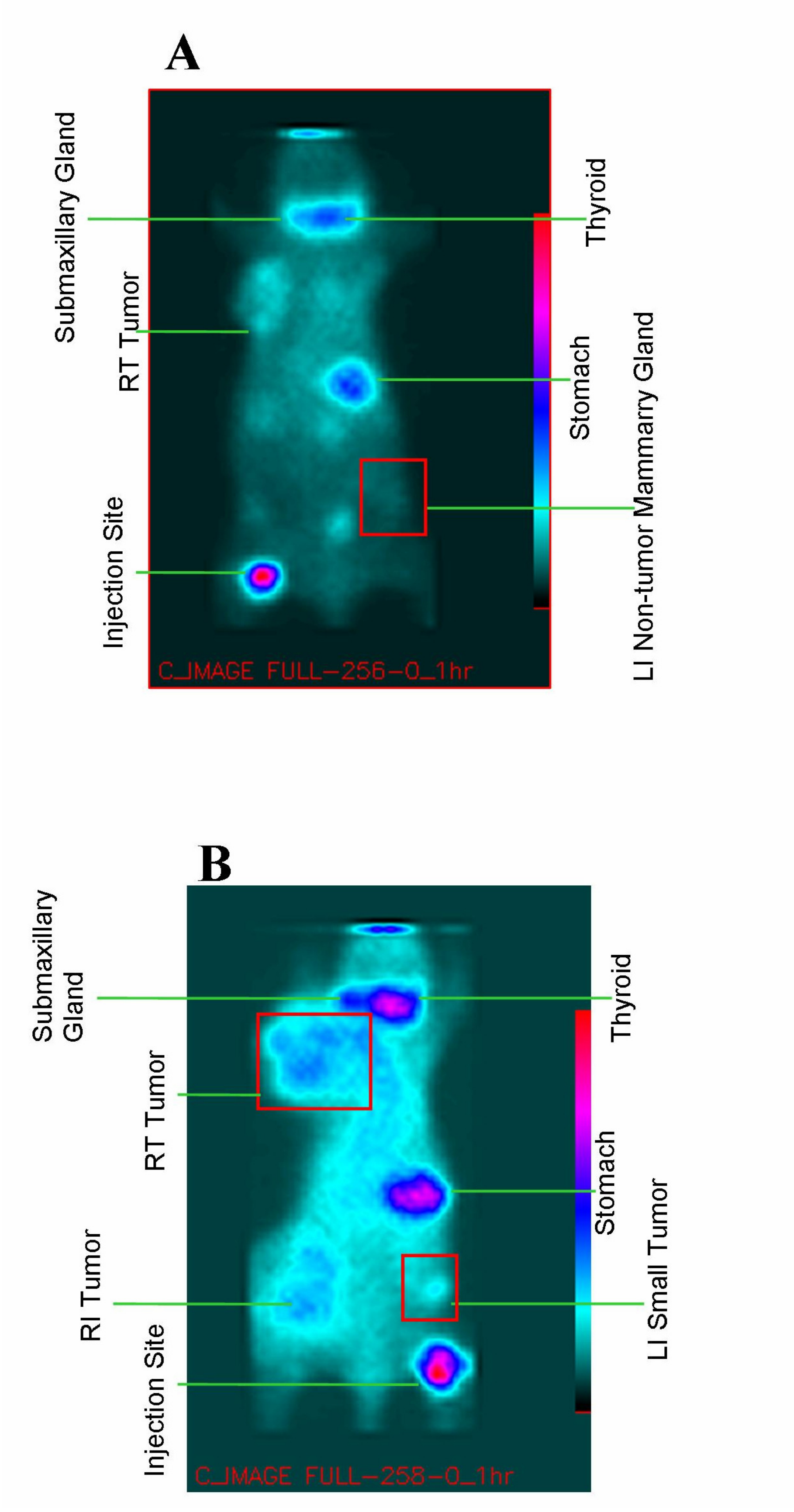
A
Submaxillary Gland
RT Tumor
Injection Site
Thyroid
Stomach
LI Non-tumor Mammary Gland
C_IMAGE FULL-256-0_1hr
B
Submaxillary Gland
RT Tumor
RI Tumor
Injection Site
Thyroid
Stomach
LI Small Tumor
C_IMAGE FULL-258-0_1hr

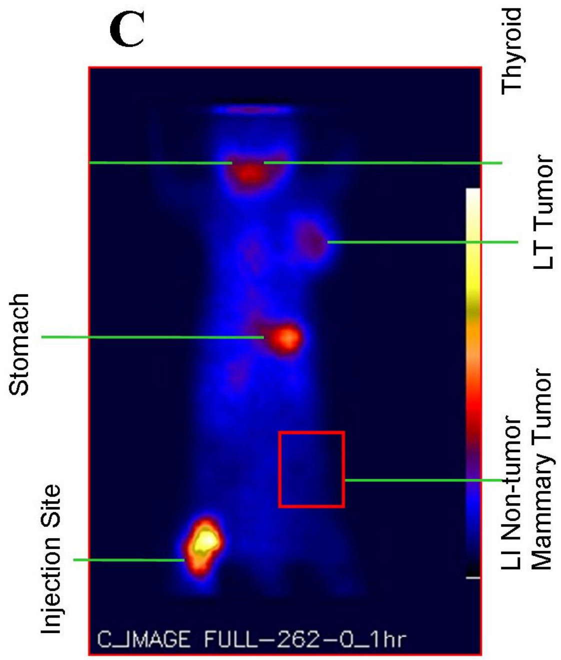
C
Thyroid
LT Tumor
Stomach
LI Non-tumor
Mammary Tumor
Injection Site
C_IMAGE FULL-262-0_1hr

D

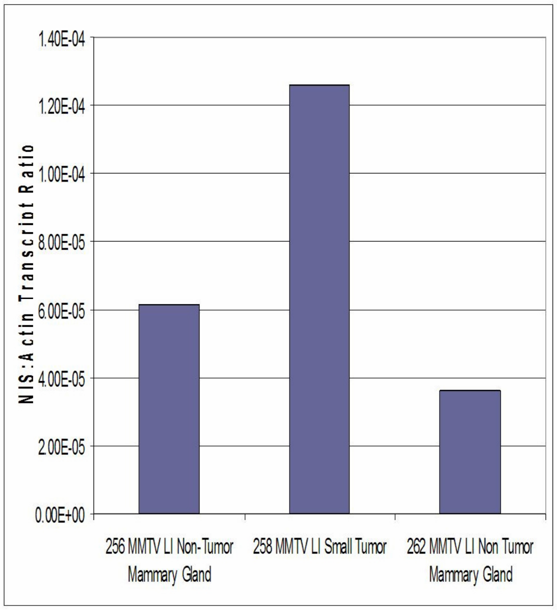
NIS:Actin Transcript Ratio
1.40E-04
1.20E-04
1.00E-04
8.00E-05
6.00E-05
4.00E-05
2.00E-05
0.00E+00
256 MMTV LI Non-Tumor Mammary Gland
258 MMTV LI Small Tumor
262 MMTV LI Non Tumor Mammary Gland

E

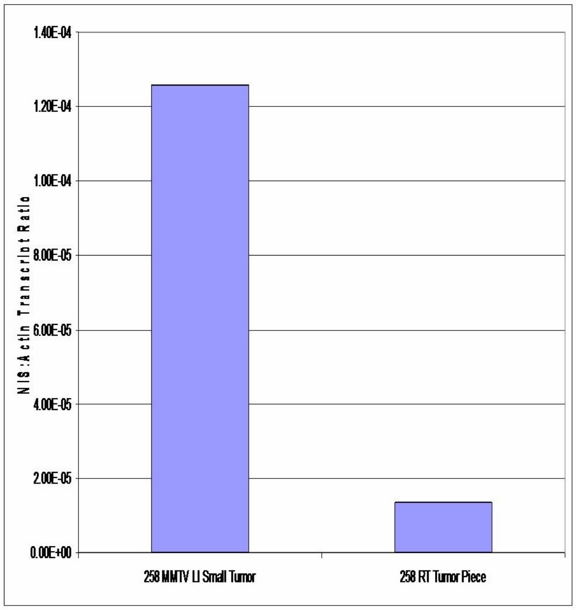
NIS:Actin Transcript Ratio
1.40E-04
1.20E-04
1.00E-04
8.00E-05
6.00E-05
4.00E-05
2.00E-05
0.00E+00
258 MMTV LI Small Tumor
258 RT Tumor Piece

Figure 9. RT-PCR for NIS mRNA expression in mammary glands of C57 mice.

RT-PCR products from whole mammary glands of a (A) nulliparous mouse (mouse 255) right axillary mammary gland, (B) previously pregnant mouse (mouse 250) right inguinal mammary gland and (C) lactating mouse (mouse 253) left axillary mammary gland were separated on 1.2% agarose gels. NIS expression is demonstrated by a band of 201 base pairs in lane 2 of each gel, as determined by comparison with 1Kb+ DNA ladder in lane 1. Lane 3 shows no RT negative controls for NIS in each RT-PCR reaction. β-actin was run in parallel as an internal control (not shown).

A

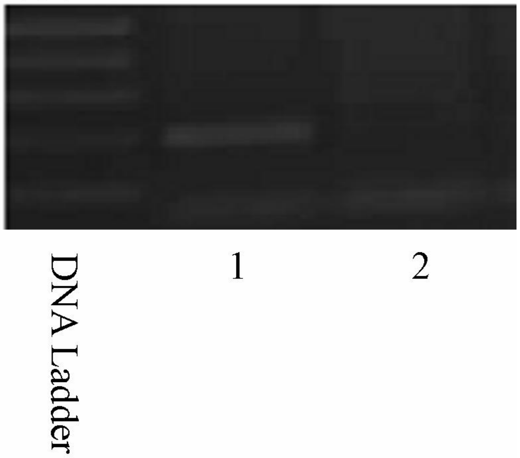

B

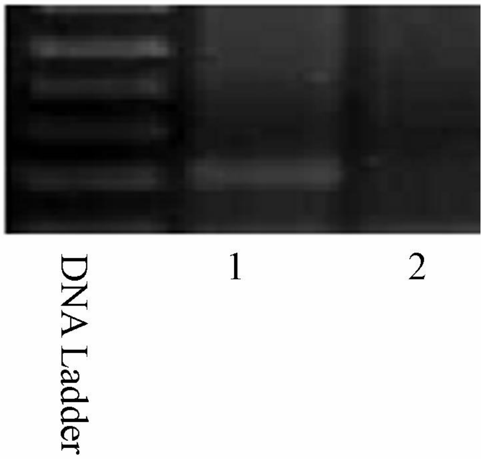

C

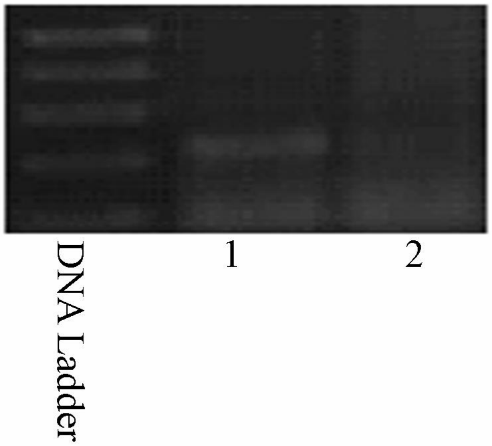

Figure 10. Comparison of radioiodide uptake and NIS mRNA level in C57 mouse mammary glands.

C57 mice were used in this comparative study to compare levels of NIS in MMTV mice with C57 mice. Lactating mice (mouse 251 and mouse 253) were imaged with the gamma camera and revealed radioiodide uptake in each mammary gland. The right axillary mammary gland of mouse 251 (A) was used for real-time RT-PCR analysis, and the left axillary mammary gland was used from mouse 253 (B), each marked with a red box. A multiparous mouse (mouse 250) which had previously been pregnant as well as a nulliparous mouse (mouse 255). Neither mouse exhibited radioiodide uptake in mammary gland regions (C and D). The right inguinal (RI) mammary gland of the multiparous mouse (mouse 250) and the right axillary (RA) mammary gland of the nulliparous mouse (mouse 255) were removed and analyzed using real-time RT-PCR Real-time RT-PCR was performed using 500 ng of total RNA extracted from each tumor piece to record levels of NIS and β-actin mRNA. The mean Ct values for each gene were converted into transcript copy number. Data are presented as a ratio of NIS: β-actin transcript copy number (E). Lactating mammary glands display more mRNA expression than multiparous or nulliparous mammary glands. Mouse 253 exhibited a large increase in NIS mRNA level, while mouse 251 showed a more modest increase over non-lactating glands.

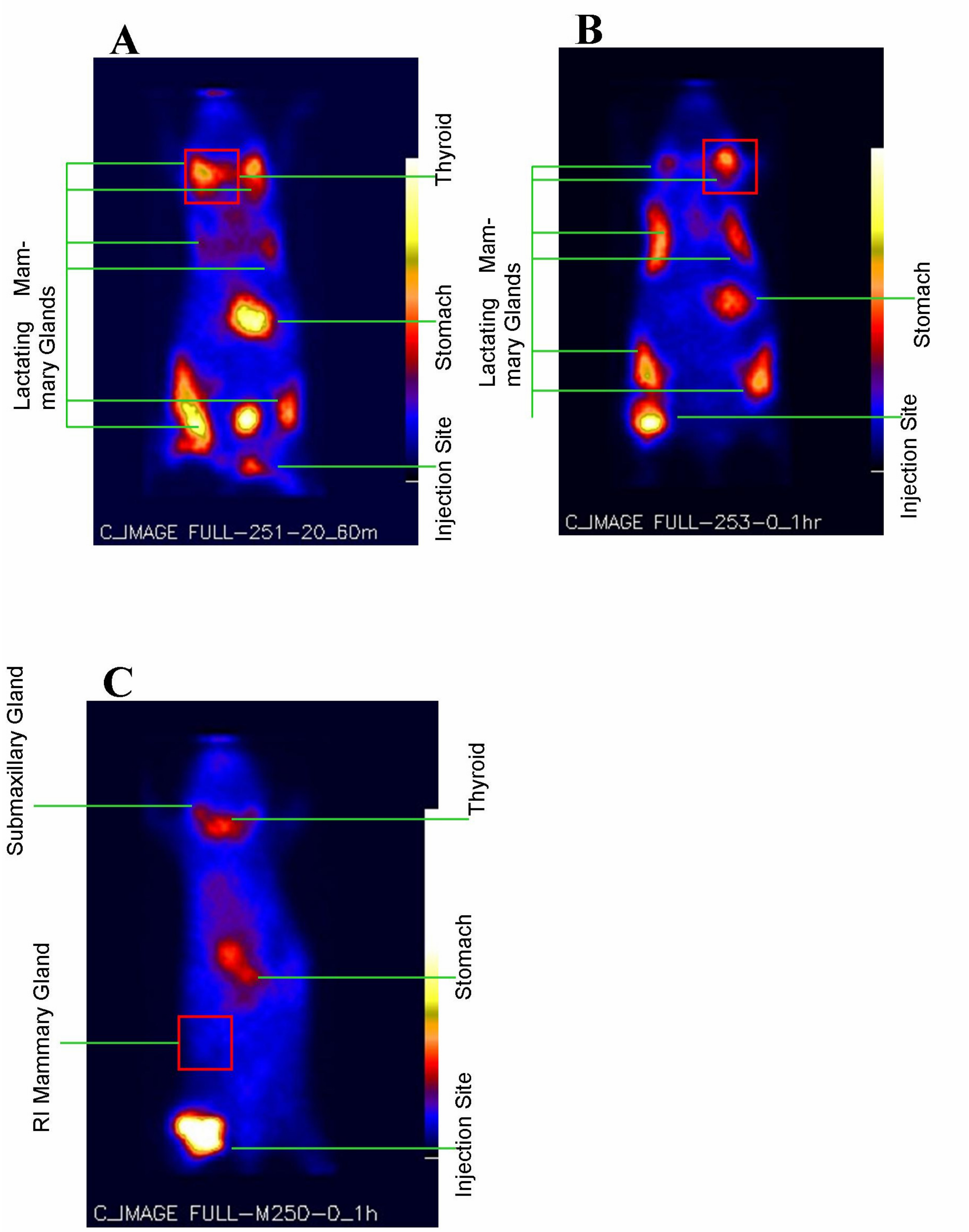
A
Lactating Mam-
mary Glands
Thyroid
Stomach
Injection Site
C_IMAGE FULL-251-20_60m
B
Lactating Mam-
mary Glands
Stomach
Injection Site
C_IMAGE FULL-253-0_1hr
C
Submaxillary Gland
Thyroid
Stomach
RI Mammary Gland
Injection Site
C_IMAGE FULL-M250-0_1h

D

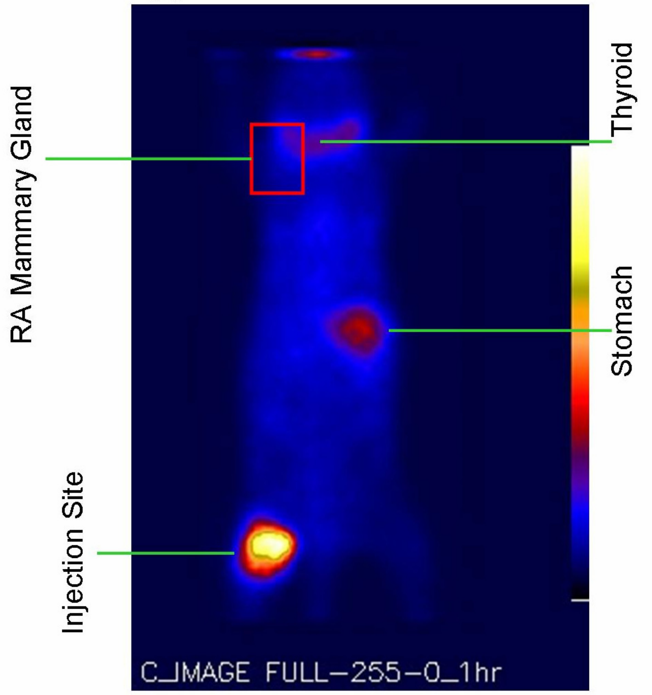
RA Mammary Gland
Thyroid
Stomach
Injection Site
C_IMAGE FULL-255-0_1hr

E

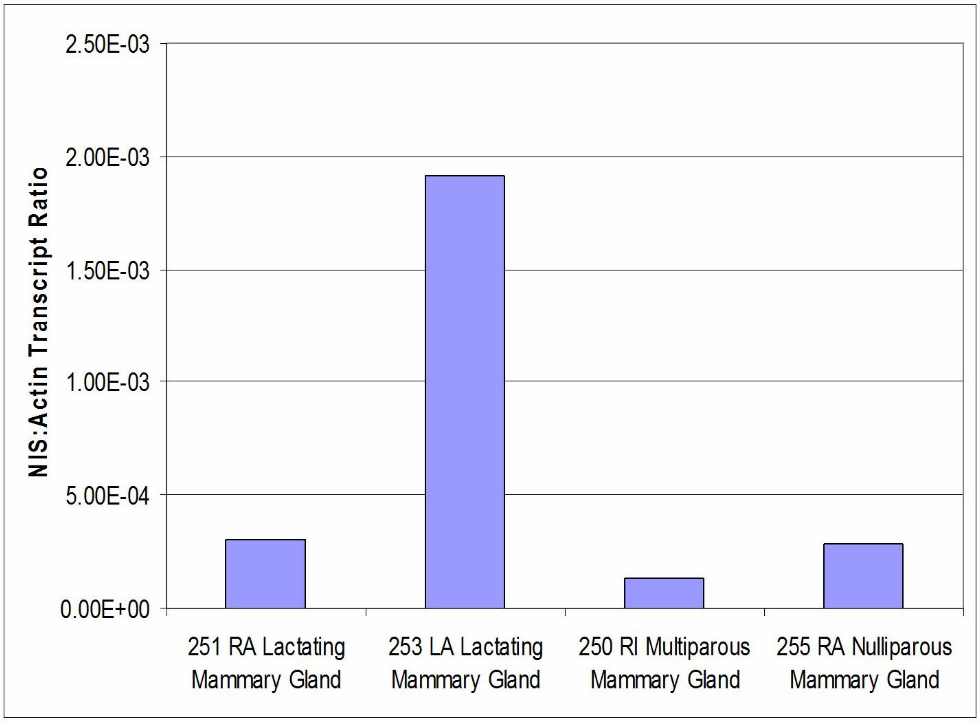
NIS:Actin Transcript Ratio
2.50E-03
2.00E-03
1.50E-03
1.00E-03
5.00E-04
0.00E+00
251 RA Lactating Mammary Gland
253 LA Lactating Mammary Gland
250 RI Multiparous Mammary Gland
255 RA Nulliparous Mammary Gland

DISCUSSION AND FUTURE DIRECTIONS

Summary of Conclusions from Results

The goal of this research was to determine if a correlation existed between NIS mRNA levels and radioiodide uptake in MMTV-induced mouse mammary tumors and non-tumor mammary glands. We hypothesized that NIS function in mammary tumors and non-tumor mammary glands is regulated primarily at the transcriptional level. We predicted that tumors or regions of tumors with high levels of radioiodide uptake would have correspondingly high levels of NIS mRNA. Previous studies of in vivo mouse models examining radioiodide uptake as mediated through NIS have shown a positive correlation between the NIS expression and radioiodide uptake (Kogai, 2004; Dwyer, 2005). However, these studies do not directly correlate amounts or patterns of radioiodide uptake with NIS mRNA quantification using real-time RT-PCR. These studies also rely on NIS expression driven by a MUC-1 promoter (Dwyer, 2005) or induced with trans-retinoic acid (tRA) treatment (Kogai, 2004) rather than endogenous NIS expression. Dwyer et al. (2005) demonstrated NIS protein expression with immunohistochemical staining prior to implantation of T47D breast cancer cells, but did not correlate radioiodide uptake with any quantitative measurement of NIS expression. Kogai et al. (2004) examined NIS expression and radioiodide uptake in a MMTV-PyVT breast cancer mouse model following treatment with tRA. tRA treatments led to increases in NIS mRNA levels as measured by quantifying the density of RT-PCR product on agarose gels. A positive correlation between increases in both expression of NIS mRNA and radioiodide uptake was observed following treatment with tRA, suggesting that NIS function is regulated at the mRNA level.

The conclusions from our research suggest that there is tentative for support for this hypothesis and previous findings in other model systems, but some contradicting results occurred. First, contradictory results were found in correlating increased NIS mRNA expression with increased radioiodide uptake. In cases such as mouse 229, an increase in NIS mRNA directly correlated with an increase in radioiodide uptake. In cases such as mouse 240, no relationship was discovered. However, there were also variations in the patterns of radioiodide uptake and morphology of the tumor, which may account for some of the lack of correlation. Second, higher NIS mRNA levels in non-tumor mammary glands was significantly correlated with increased radioiodide uptake, suggesting that NIS is regulated at the transcriptional level in early tumor development.

Whether NIS mRNA levels correlated with radioiodide uptake seemed related to variations in the pattern of radioiodide uptake in mammary tumors. Tumors displaying a center-to-edge pattern of uptake (mouse 209 and mouse 229) possessed a positive correlation between increased NIS mRNA and increased radioiodide uptake, while tumors with a multi-spot pattern of radioiodide uptake (mouse 240) did not show this correlation. Our ROI analysis data suggest that tumors accumulating radioiodide in a center-to-edge pattern are younger than those exhibiting a multi-spot pattern. This presents the possibility that as tumors age there is an altered iodide metabolism involving NIS mRNA regulation changes as well. NIS expression and iodide uptake capability has been shown by other to be downregulated in this manner during thyroid cancer (Schlumberger, 2007), which supports the possibility that a similar change in expression and uptake occurs in breast cancer progression. Additionally, the variable morphology of tumors and tumor pieces appeared to relate to whether NIS mRNA and radioiodide uptake positively correlated. Regions of dense, white tissue more often exhibit a strong correlation between NIS mRNA and radioiodide uptake than regions of tumor containing blood-filled, necrotic tissue.

NIS mRNA Upregulation during Early Tumor Development

Mammary glands without palpable tumors (mouse 256, mouse 258, mouse 262) showed an increase in NIS mRNA that was positively correlated with an increase in radioiodide uptake. From this finding, we propose that NIS upregulation in early tumor development can be effectively imaged using the gamma camera at a stage in which the tumor is non-palpable. Zuckier et al. (2001) and Tazebay et al. (2000) report that mammary gland NIS is upregulated in proliferating breast tissue. In our MMTV mouse, spontaneously mammary tumor formation and proliferation appears to trigger this NIS upregulation. Because of the correlation between NIS mRNA and radioiodide uptake in these tissues, we can image the presence of proliferating mammary tissue using radioiodide. Additionally, the high resolution of the small animal gamma camera further augments the capacity for NIS to serve as a reporter gene for early detection of breast cancer (Dingli, 2003). The measurement of increases in endogenous NIS mRNA as a reporter gene combined with the potential to image non-palpable tumors using the gamma camera presents a method of early breast cancer detection which surpasses the resolution of currently available gamma cameras (Dingli, 2003), while maintaining specificity for breast cancer tissue.

Differential Regulation of NIS Expression and Function in Breast Cancer

Our studies included both tumors which showed correlation between NIS mRNA and functional iodide uptake and tumors which showed no correlation. This finding suggests that NIS can be regulated on the transcriptional level as well as translational and/or post-translational levels in breast cancer tissue. The exact molecular mechanism of NIS induction and activation has yet to be described, however (Arturi, 2005). Studies have indicated multiple levels of NIS regulation, but these are limited to in vitro experiments using the human adenocarcinoma cell line MCF-7 (Dohan, 2006).

In our samples in which increased NIS mRNA expression correlated with increased radioiodide uptake on gamma camera images, regulation on the transcriptional level is suggested. Multiple factors have been shown to induce NIS mRNA expression in vitro. Hormonal regulation by insulin, IGF-I, and IGF-II plays a role in mammary cell proliferation. Addition of these hormones to MCF-7 cells also caused an increase in NIS mRNA and protein in studies by Arturi et al. (2005). However, Dohan et al. (2006) were unable to reproduce these findings in the absence of trans-retinoic acid (tRA). Lactogenic hormones also have been suggested to play a role in NIS activation. Prolactin, acting through MAPK or PI3K, and oxytocin, acting through PKC and MAPK, have each been implicated in NIS signal transduction, but neither pathway has been fully characterized in NIS activation in breast cancer (Knostman, 2004). Knostman et al. (2004) also investigated the role of cAMP in NIS activation in breast cancer. Treating cells with cAMP resulted in a significant increase in NIS mRNA and promoter activity, but did not result in increased protein expression or functional iodide uptake. This evidence suggests that while cAMP is able to drive NIS protein and functional iodide uptake in thyroid cells, its effects are limited to the transcriptional level in breast cancer. Because MCF-7 cells express a low basal level of NIS, factors to increase expression, such as tRA, have been the focus of many studies (Kogai, 2004; Kogai 2005; Dohan, 2006). Kogai et al. (2004) found that induction of NIS expression in MCF-7 cells requires tRA treatment, and in 2005 showed that addition of dexamethasone further increases NIS at the transcriptional level.

In our MMTV tumors which exhibited no correlation between NIS mRNA expression and NIS functional activity by uptake of radioiodide, we suggest that regulation occurred at a post-transcriptional level. Kogai et al. (2004) showed evidence for this type of regulation in a time course treatment of MCF-7 cell xenografts with tRA. After day 2, xenografts exhibited the maximum level of NIS mRNA expression throughout the time course of tRA treatment, while the maximum levels of both protein expression and iodide uptake occurred on day 5. This finding supports our finding of no correlation between NIS mRNA and radioiodide uptake in some tumor tissues. Kogai suggests that this lag time may be due to NIS processing. Mammary gland NIS is known to be glycosylated. NIS is phosphorylated in thyroid cells, but it is unknown if phosphorylation of NIS is required for function in breast cancer. Membrane targeting is also thought to play a role in this lag time between NIS mRNA expression and functional iodide uptake.

In addition to this study by Kogai, other studies have implicated other signaling and regulatory mechanisms. Knostman et al. (2004) showed that PI3K alone can induce NIS function, while, cAMP leads only to increases in mRNA. This finding demonstrates the multiple pathways through which NIS is activated in breast cancer. Also, Dohan, et al. (2006) have shown that in MCF-7 mammary tumor cells, unlike in thyroid cells, increased iodide levels do not have the effect to downregulate iodide transport. This finding suggests evidence for a different pathway of negative feedback control in breast cancer, if not a complete lack of negative feedback.

Regulation of NIS expression and function on the transcriptional and post-transcriptional levels has been shown in MCF-7 breast cancer cells. In our experiments, we see evidence that supports differential regulation in our MMTV-mouse model. Tumors showing a correlation between NIS mRNA expression and radioiodide uptake suggest that regulation in these tissues occurs primarily at the transcriptional level. While the tumors that show a lack of correlation between increases in mRNA and increases in radioiodide uptake suggest that the processes seen in Kogai et al. (2004), with an initial increase in mRNA level is followed by a lag time for post-transcriptional processing before NIS protein and iodide uptake are present, are occurring. In our experience, we see evidence for both models with the correlation between real-time RT-PCR, immunohistochemical, and gamma camera imaging data. Clearly there is a need for further investigation both in MCF-7 cell lines as well as with animal models to more completely understand where NIS regulation occurs in breast cancer.

Future Directions

While our results indicate that in MMTV-induced mouse mammary tumors NIS mRNA is correlated with increased radioiodide uptake in younger dense tumors, it does not seem to be similarly correlated in older more diffuse tumors. A significantly increased sample size of imaged mice with NIS mRNA measured by real-time RT-PCR and more precisely correlated with location within the tumor will be necessary to make more definitive conclusions.

A method to further examine the upregulation of NIS mRNA in developing mammary tumors should include imaging and real-time RT-PCR on MMTV-infected mice which lack tumors. NIS expression compared with radioiodide uptake in each mammary gland should be measured in mice at ages in which the probability of developing a tumor is high.

In order to more completely understand the regulation of NIS expression in our MMTV-model, we should investigate expression patterns of genes which are key regulators of NIS function. Such genes would include ER, and PRL-R. These studies should be performed at the level of mRNA, protein, and function through real-time RT-PCR, immunohistochemistry, and gamma camera imaging, respectively. Once correlative relationships between NIS and proteins which have a key role in its regulation are found in MMTV-mice, the study could continue in primary cultures of MMTV-cells, which have already been established. In these studies, we can perform immunocytochemistry should be used to determine the percentage of cells which express both NIS and those proteins which regulate its function.

To determine more precisely the signaling pathway that regulates NIS mRNA expression in our MMTV model, we should employ real-time RT-PCR on primary cell cultures following treatments with inhibitors for suspected signaling pathways. First, basal NIS expression should be quantified as transcripts per cell. Second, treatments with inhibitors known to block the function of implicated signaling pathways, such as through cAMP and PI3K, should be used in treatments of cells to determine if blocking these pathways decreases amount of NIS mRNA. Finally, if one or multiple pathways are implicated in affecting regulation of NIS mRNA, radioiodide uptake in these cells can be measured to determine if the alteration of these pathways prevents functional iodide uptake as well.

In addition to experiments which investigate the question of NIS regulation in our MMTV model, we are interested in the potential of NIS as a marker gene for breast cancer. Using microarray with pre-designed breast cancer gene chips and real-time RT-PCR, we will investigate what cancer genes are overexpressed in conjunction with NIS. While NIS has shown to be an effective imaging reporter gene (Dingli, 2003), we aim to evaluate its potential as a marker gene for a more specific gene expression profile. This investigation will contribute not only to our understanding of genes which are co-expressed with NIS, but will also indicate a potential to use gamma camera imaging with radioiodide for molecular imaging that can provide a profile of global gene expression within a tumor.

REFERENCES

Allred DC, Brown P, Medina D. 2004. The origins of estrogen receptor alpha-positive and estrogen receptor alpha-negative human breast cancer. *Breast Cancer Res* 6:240-245.

Arturi F, Ferretti E, Presta I, Mattei T, Scipioni A, Scarpelli D, Bruno R, Lacroix L, Tosi E, Gulino A, Russo D, Filetti S. 2005. Regulation of iodide uptake and sodium/iodide symporter expression in the MCF-7 human breast cancer cell line. *Journal of Clinical Endocrinology* 90(4):2321-2326.

Benard F, Turcotte E. 2005. Imaging in breast cancer: Single-photon computed tomography and positron-emission tomography. *Breast Cancer Research* 7:153-162.

Bradley EL, Cella J, Majewski S, Popov V, Qian J, Saha MS, Smith MF, Weisenberger AG, Welsh RE. 2006. A Compact Gamma Camera for Biological Imaging. *IEEE Transactions on Nuclear Medicine* 53(1):59-65.

Brem FR, Petrovitch I, Rapelyea JA, Young H, Teal C, Kelly T. 2007. Breast-Specific Gamma Imaging with ^{99m}Tc-Sestamibi and Magnetic Resonance Imaging in the Diagnosis of Breast Cancer—A Comparative Study. *The Breast Journal* 13(5):465-469.

Cardiff RD, Wellings SR. 1999. The Comparative Pathology of Human and Mouse Mammary Glands. *Journal of Mammary Gland Biology and Neoplasia* 4(1):105-122.

Cardiff RD, Kenney N. 2007. Mouse Mammary Tumor Biology: A Short History. *Adv Cancer Res.* 98:53-116.

Carrasco N. 1993. Iodide transport in the thyroid gland. *Biochim Biophys Acta* 1154:65–82.

Cho JY, Leveille R, Kao R, Rousset B, Parlow AF, Burak Jr WE, Mazzaferri EL, Jhiang SM. 2000. Hormonal regulation of radioiodide uptake activity and Na^+/I^- symporter expression in mammary glands. *J Clin Endocrinol Metab* 85:2936–2943.

Ciarloni L, Mallepell S, Brisken C. 2007. Amphiregulin is an essential mediator of estrogen receptor α function in mammary gland development. *PNAS* 104(13):5455-5460.

Dai G, Levy O, Carrasco N. 1996. Cloning and characterization of the thyroid iodide transporter. *Nature* 379:458–460.

Dayem M, Basquin C, Navarro V, Carrier P, Marsault R, Chang P, Huc S, Darrouzet E, Lindenthal S, Pourcher T. 2008. Comparison of expressed human and mouse sodium/iodide symporters reveals differences in transport properties and subcellular localization. *Journal of Endocrinology* 197:95-109.

Dingli D, Russel SJ, Morris JC. 2003. In vivo imaging and tumor therapy with the sodium iodide symporter. *Journal of Biological Chemistry* 90:1079-1086.

Dohan O, De la Vieja A, Paroder V, Riedel C, Artani M, Reed M, Ginter CS & Carrasco N. 2003a. The sodium/iodide symporter (NIS): characterization, regulation, and medical significance. *Endocrine Reviews* 24:48–77.

Dohan O and Carrasco N. 2003b. Advances in Na+/I- symporter (NIS) research in the thyroid and beyond. *Molecular and Cellular Endocrinology* 213:59-70.

Dohan O, De la Vieja A, Carrasco N. 2006. Hydrocortisone and purinergic signaling stimulate sodium/iodide symporter (NIS)- mediated iodide transport in breast cancer cells. *Molecular Endocrinology* 20(5):1121-1137.

Dwyer RM, Bergert ER, O'Connor MK, Gendler SJ, Morris JC. 2005. In vivo radioiodide imaging and treatment of breast cancer xenographs after MUC1-driven expression of the sodium iodide symporter. *Clinical Cancer Research* 11:1483-1489.

Elmore JG, Armstrong K, Lehman CD, Fletcher SW. 2005. Screening for breast cancer. *JAMA* 293(10):1245-1256.

Esserman L, Wolverton D, Hylton N. 2002. Magnetic resonance imaging for primary breast cancer management: current role and new applications. *Endocrine-related Cancer* 9:141-153.

Fey A, Eichler S, Flavier S, Christen R, Hofle MG, Guzman CA. 2004. Establishment of a real-time PCR-based approach for accurate quantification of bacterial RNA targets in water, using *Salmonella* as a model organism. *Appl Environ Microbiol* 70(6):3618-3623.

Fowler AM, Alarid ET. 2007. Amping up estrogen receptors in breast cancer. *Breast Cancer Research* 9:305.

Fronhoffs S, Totzke G, Stier S, Wernert N, Rothe M, Bruning T, Koch B, Sachinidis A, Vetter H, Ko Y. 2002. A method for the rapid construction of cRNA standard curves in quantitative real-time reverse transcription polymerase chain reaction. *Molecular and Cellular Probes* 16:99-110.

Golovkina TV, Piazzon I, Nepomnaschy I, Buggiano V, Olano Vela M, Ross SR. 1997. Generation of a Tumorigenic Milk-Borne Mouse Mammary Tumor Virus by Recombination between Endogenous and Exogenous Viruses. *Journal of Virology* 71(5):3895-3903.

Hammond WT, Bradley EL, Welse RE, Qian J, Weisenberger AG, Smith MF, Majewski S, Saha MS. 2007. A gamma camera re-evaluation of potassium iodide blocking efficiency in mice. *Health Phys* 92(4):396-406.

Hylton N. 2005. Magnetic resonance imaging of the breast: Opportunities to improve breast cancer management. *Journal of Clinical Oncology* 23(8):1678-1684.

Ikdea K, Inoue S. 2004. Estrogen receptors and their downstream targets in cancer. *Arch Histol Cytol* 67(5):435-442.

Jemal A, Siegal R, Ward E, Murray T, Xu J, Thun MJ. 2007. Cancer Statistics 2007. *CA Cancer J Clin* 57:43-66.

Kapp AV, Jeffrey SS, Langerod A, Borresen-Dale AL, Han W, Noh DY, Bukholm IR, Nicolau M, Brown PO, Tibshirani R. 2006. Discovery and validation of breast cancer subtypes. *BMC Genomics* 7:231.

Kilbane MT, R. A. Ajjan, A. P. Weetman, R. Dwyer, E. W. M. McDermott, N. J. O'Higgins, P. P. A. Smyth. 2000. Tissue iodine content and serum-mediated ^{125}I uptake-blocking activity in breast cancer. *J Clin Endocrinol Metab* 85:1245–1250.

Knostman KA, Cho JY, Ryu KY, Lin X, McCubrey JA, Hla T, Liu CH, Di Carlo E, Keri R, Zhang M. 2004. Signaling through 3',5'-cyclic adenosine monophosphate and phosphoinositide-3 kinase induces sodium/iodide symporter expression in breast cancer. *Journal of Clinical Endocrinology and Metabolism* 89:5196–5203.

Kogai T, Schultz JJ, Johnson LS, Huang M & Brent GA. 2000. Retinoic acid induces sodium/iodide symporter gene expression and radioiodide uptake in the MCF-7 breast cancer cell line. *PNAS* 97: 8519–8524.

Kogai T, Kanamoto Y, Che LH, Taki K, Moatamed F, Schultz JJ, Brent GA. 2004. Systemic retinoic acid treatment induces sodium/iodide symporter expression and radioiodide uptake in mouse breast cancer models. *Cancer Research* 64:415–422.

Kogai T, Kanamoto Y, Li AI, Che LH, Ohashi E, Taki K, Chandraratna RA, Saito T, Brent GA. 2005. Differential regulation of sodium/iodide symporter gene expression by nuclear receptor ligands in MCF-7 breast cancer cells. *Endocrinology* 146(7):3059-3069.

Lee C, Lee S, Shin SG, Hwang S. 2008. Real-time PCR determination of rRNA gene copy number: Absolute and relative quantification assays with Escherichia coli. *Appl Microbiol and Biotechnol* 78:371-376.

Lee S, Medina D, Tsimelzon A, Mohsin SK, Mao S, Wu Y, Allred DC. 2007. Alterations of gene expression in the development of early hyperplastic precursors of breast cancer. *The American Journal of Pathology* 171(1):252-262.

Levy O, De la Vieja A, Carrasco N. 1998. The Na^+/I^- symporter (NIS): recent advances. *J Bioenerg Biomemb* 30:195–206.

Lyons SK. 2005. Advances in imaging mouse tumour models in vivo. *J Pathol* 205:194-205.

Ma L, Gauville C, Berthois Y, Millot G, Johnson GR, Calvo F. 1999. Antisense expression for amphiregulin suppresses tumorigenicity of a transformed human breast epithelial cell line. *Oncogene* 18:6513-6520.

Mankoff DA. 2004. Radiotracer breast cancer imaging: Beyond FDG and MIBI. *Physica Medica* 21(Supp1):12-16.

Moon, D.H., Lee, S.J., Park, K.Y., Park, K.K., Ahn, S.H., Pai, M.S., Chang, H., Lee, H.K. and Ahn, I.M. 2001. Correlation between 99mTc-pertechnetate uptakes and expressions of human sodium iodide symporter gene in breast tumor tissues. *Nucl. Med. Biol* 28:829–834.

Nahmias C. 2002. Molecular imaging: the next frontier. *Can Assoc Radiol J* 53(5):255-257.

Normano N, Selvam MP, Qi CF, Saeki T, Johnson G, Kim N, Ciardiello F, Shoyab M, Plowman G, Brandt R, Todaro G, Salomon DS. 1994. Amphiregulin as an autocrine growth factor for c-Ha-*ras*- and c-*erbB-2*-transformed human mammary epithelial cells. *Proc. Natl. Acad. Sci. USA* 91:2790-2794.

Quon A, Gambhir SS. 2005. FDG-PET and Beyond: Molecular Breast Cancer Imaging. *J Clin Oncol* 23:1664-1673.

Perron B, Rodriguez AM, Pourcher T. 2001. Cloning of the mouse sodium iodide symporter and its expression in the mammary gland and other tissues. *Journal of Endocrinology* 170:185-196.

Politi K, Feirt N, Kitajewski J. 2004. Notch in mammary gland development and breast cancer. *Seminars in Cancer Biology* 14:341-347.

Riesco-Eizaguirre G, Santisteban P. 2006. A perspective view of sodium iodide symporter research and its clinical implications. *Eur J Endocrinol* 155(4):495-512.

Sambrook J, Russell DW. 2001. *Molecular Cloning: A Laboratory Manual*. Cold Spring Harbor, New York: Cold Spring Harbor Laboratory Press.

Schillaci O, Cossu E, Romano P, Sanso C, Danieli R, Granai AV, Caravaglia G, Pisolese CA, Buonomo O, Simonetti G. 2006. High-resolution gamma-camera for molecular breast imaing: first clinical results. *Physica Medica* 21(S1):121-124.

Schipper ML, Riese CGU, Seitz S, Weber A, Behe M, Schurrat T, Schramm N, Keil B, Alfke H, Behr TM. 2007. Efficacy of ^{99m}Tc pertechnetate and ^{131}I radioisotope therapy in sodium/iodide symporter (NIS)-expressing neuroendocrine tumors in vivo. *Eur J Nucl Med Mol Imaging* 34:638-650.

Schlumberger M, Lacroix L, Russo D, Filetti S, Bidart JM. 2007. Defects in iodide metabolism in thyroid cancer and implications for the follow-up and treatment of patients. *Nature Clinical Practice: Endocrinology & Metabolism* 3:260-269.

Schoder H, Gonen M. 2007. Screening for cancer with PET and PET/CT: Potential and limitations. *Journal of Nuclear Medicine* 48(1):4S-18S.

Sive HL, Grainger RM, Harland RM. 2000. *Early Development of Xenopus laevis: A Laboratory Manual.* Cold Spring Harbor, New York: Cold Spring Harbor Laboratory Press.

Smanik PA, Ryu K-Y, Theil KS, Mazzaferri EL, Jhiang SM. 1997. Expression, exon-intron organization, and chromosome mapping of the human sodium iodide symporter. *Endocrinology* 138:3555–3558.

Spitzweg, C, Joba W, Eisenmenger W, Heufelder AE. 1998. Analysis of human sodium iodide symporter gene expression in extrathyroidal tissues and cloning of its complementary DNA form salivary gland, mammary gland, and gastric mucosa. *J Clin Endocrinol Metab* 83:1746–1751

Tanosaki S, Ikezoe T, Heaney A, Said JW, Dan K, Akashi M, Koeffler HP. 2003. Effect of ligands of nuclear hormone receptors on sodium/iodide symporter expression and activity in breast cancer cells. *Breast Cancer Research and Treatment* 79:335-345.

Tazebay UH, Wapnir IL, Levy O, Dohan O, Zuckier LS, Zhao QH, Deng HF, Amenta PS, Fineberg S, Pestell RG, Carrasco N. 2000. The mammary gland iodide symporter is expressed during lactation and in breast cancer. *Nat Med* 6:871–878.

Torigian DA, Huang SS, Houseni M, Alavi A. 2007. Functional imaging of cancer with emphasis on molecular techniques. *CA Cancer J Clin* 57:206-224.

Wapnir IL, van de Rijn M, Nowels K, Amenta PS, Walton K, Montgomery K, Greco RS, Dohan O, Carrasco N. 2003. Immunohistochemical profile of the sodium/iodide symporter in thyroid, breast, and other carcinomas using high density tissue microarrays and conventional sections. *J Clin Endocrinol Metab* 88:1880–1888.

Wapnir IL, Goris M, Yudd A, Dohan O, Adelman D, Nowels K, Carrasco N. 2004. The Na+/I- Symporter mediates iodide uptake in breast cancer metastases and can be selectively down-regulated in the thyroid. *Clinical Cancer Research* 10:4294-4302.

Weisenberger AG, Wojcik R, Bradley EL, Brewer P, Majewski S, Qian J, Ranck A, Saha MS, Smith K, Smith MF, Welsh RE. 2003. SPECT-CT system for small animal imaging. *IEEE Transactions on Nuclear Science* 50(1):74-79.

Wright H, Listinsky J, Rim A, Chellman-Jeffers M, Patrick R, Rybicki L, Kim J, Crowe J. 2005. *The American Journal of Surgery* 190:572-575.

Zuckier LS, Dadachova E, Dohan O, Carrasco N. 2001. The Endogenous mammary gland Na^+/I^- symporter may mediate effective radioiodide therapy in breast cancer. *Journal of Nuclear Medicine* 42(6)987.

APPENDIX

Real-time RT-PCR Data Plots

Mouse 240-3 and 209-1

Current Date: **02-Apr-08 02:12 PM**
Data generated on: **02-Apr-08 at 09:46 AM**.

Optical data file name: **Data 02-Apr-08 0946.opd**
Plate Setup file used: **sassamples.pts**
Protocol file used: **sasnisprobes.tmo**

PCR Amp/Cycle Graph for FAM-490

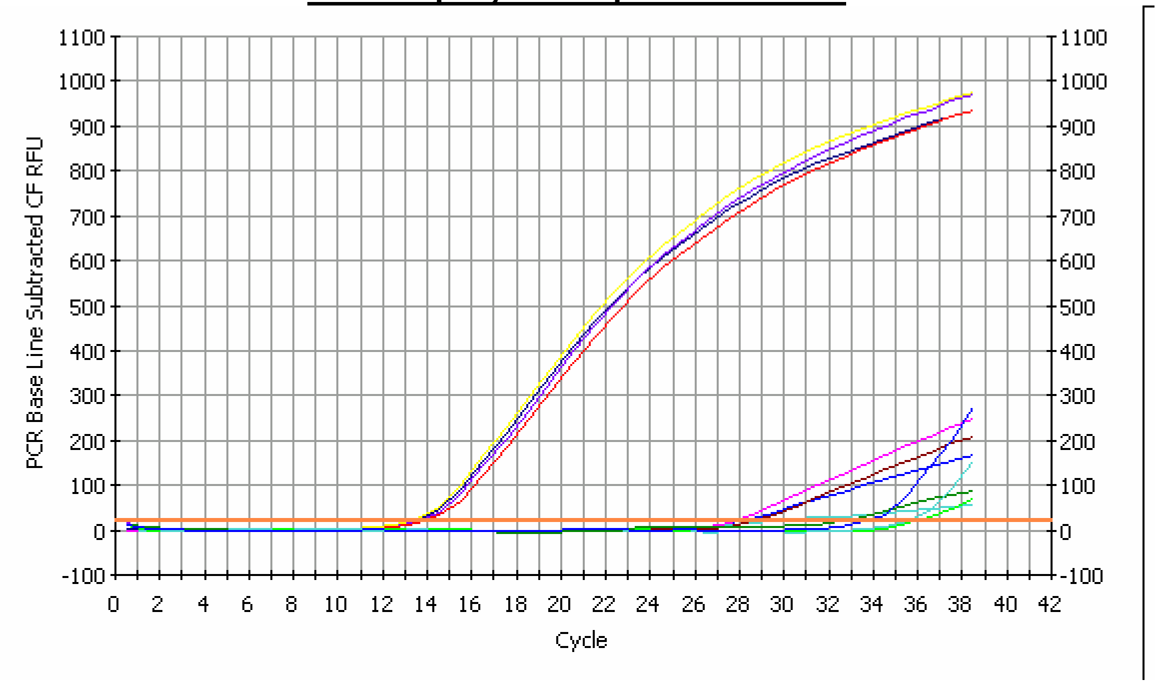

Data Analysis Parameters

Calculated threshold using the **maximum curvature approach** is **22.5**.
Per-well baseline cycles have been determined automatically.
Data analysis window is set at **95.00%** of a cycle, centered at **end** of the cycle.
Weighted Mean digital filtering has been applied. Global filtering is **off**.

PCR Quantification Spreadsheet Data for FAM-490

Well	Identifier	Ct	Setpoint
B02	240n1	29.9	
B03	209n1	28.1	
C02	240n2	27.9	
C03	209n2	28.8	
D02	240a1	13.5	
D03	209a1	13.7	
E02	240a2	13.3	
E03	209a2	14	
F02	240n noRT	36.1	
F03	209n noRT	32.8	
G02	240a noRT	35.7	
G03	209a noRT	33.7	

Mouse 168, 240-1 and 240-2

Current Date: **02-Apr-08 08:42 PM**
Data generated on: **02-Apr-08 at 06:16 PM**.

Optical data file name: **Data 02-Apr-08 1815.opd**
Plate Setup file used: **sassamples.pts**
Protocol file used: **sasnisprobes.tmo**

PCR Amp/Cycle Graph for FAM-490

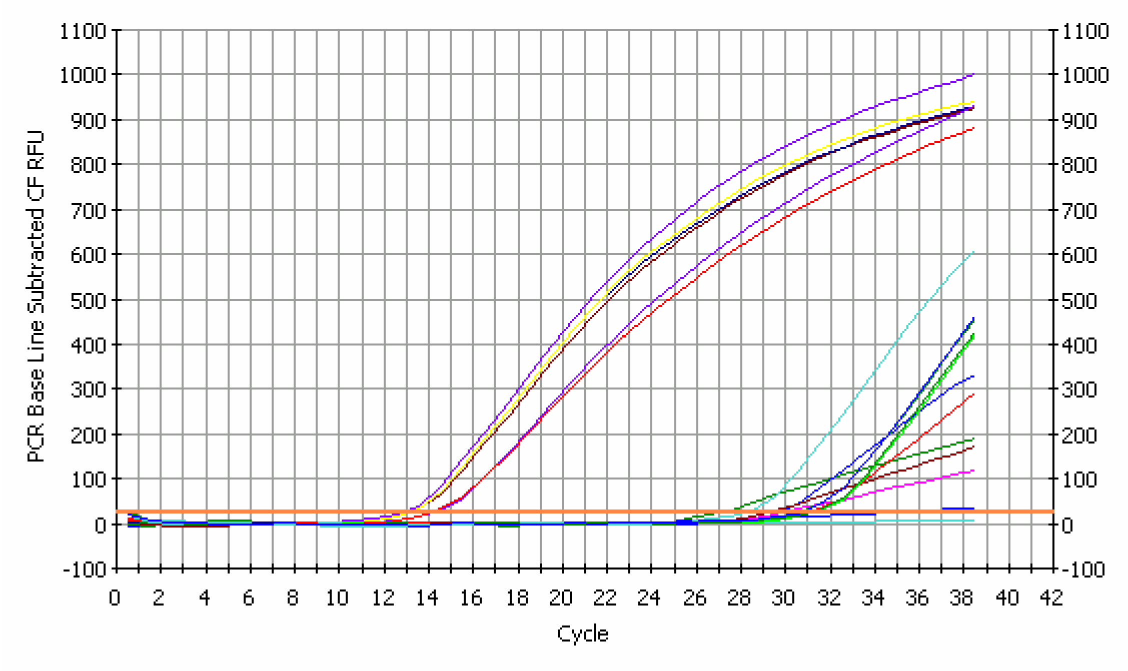

Data Analysis Parameters

Calculated threshold using the **maximum curvature approach** is **25.5**.
Per-well baseline cycles have been determined automatically.
Data analysis window is set at **95.00%** of a cycle, centered at **end** of the cycle.
Weighted Mean digital filtering has been applied. Global filtering is **off**.

PCR Quantification Spreadsheet Data for FAM-490

Well	Identifier	Ct	Setpoint
B01	168n1	27.1	
B02	2401n1	N/A	
B03	2402n1	34.4	
C01	168n2	29.8	
C02	2401n2	30	
C03	2402n2	29.3	
D01	168a1	13.2	
D02	2401a1	13	
D03	2402a1	14.3	
E01	168a2	12.7	
E02	2401a2	13.1	
E03	2402a2	14.1	
F01	168n noRT	31	
F02	2401n noRT	31.3	
F03	2402n noRT	30.7	
G01	168a noRT	31.2	
G02	2401a noRT	28.3	
G03	24029a noRT	30.8	

Mouse 209-2, 209-3, and 209-4

Current Date:	**05-Apr-08 03:57 PM**
Data generated on:	**05-Apr-08 at 01:29 PM**.
Optical data file name:	**Data 05-Apr-08 1328.opd**
Plate Setup file used:	**sassamples.pts**
Protocol file used:	**sasnisprobes.tmo**

PCR Amp/Cycle Graph for FAM-490

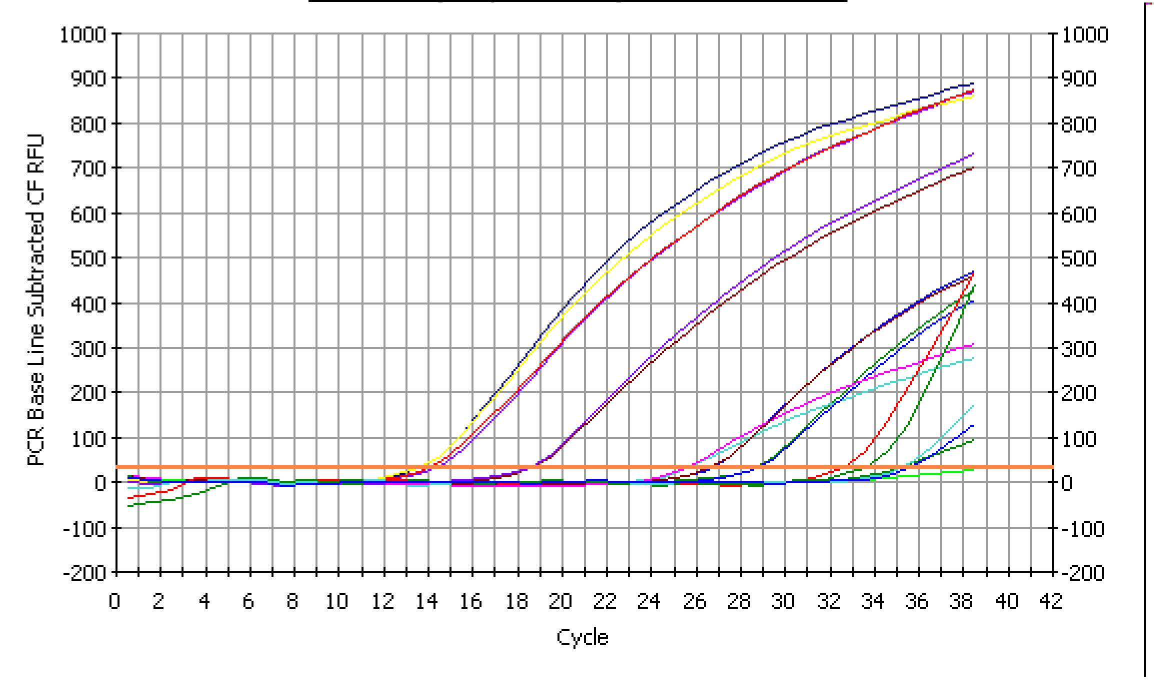

Data Analysis Parameters

Calculated threshold using the **maximum curvature approach** is **32.9**.
Per-well baseline cycles have been determined automatically.
Data analysis window is set at **95.00%** of a cycle, centered at **end** of the cycle.
Weighted Mean digital filtering has been applied. Global filtering is **off**.

PCR Quantification Spreadsheet Data for FAM-490

Well	Identifier	Ct	Setpoint
B01	2n1	28.7	
B02	3n1	25.6	
B03	4n1	26.7	
C01	2n2	28.7	
C02	3n2	25.5	
C03	4n2	26.6	
D01	2a1	18.6	
D02	3a1	13.6	
D03	4a1	14.3	
E01	2a2	18.6	
E02	3a2	13.6	
E03	4a2	14	
F01	2n noRT	32.5	
F02	3n noRT	N/A	
F03	4n noRT	35.1	
G01	2a noRT	33.5	
G02	3a noRT	35.2	
G03	4a noRT	35.6	

Mouse 240-4, 240-5, and 240-Thyroid

Current Date:	**07-Apr-08 03:15 PM**
Data generated on:	**07-Apr-08 at 12:53 PM**.
Optical data file name:	**Data 07-Apr-08 1252.opd**
Plate Setup file used:	**sassamples.pts**
Protocol file used:	**sasnisprobes.tmo**

PCR Amp/Cycle Graph for FAM-490

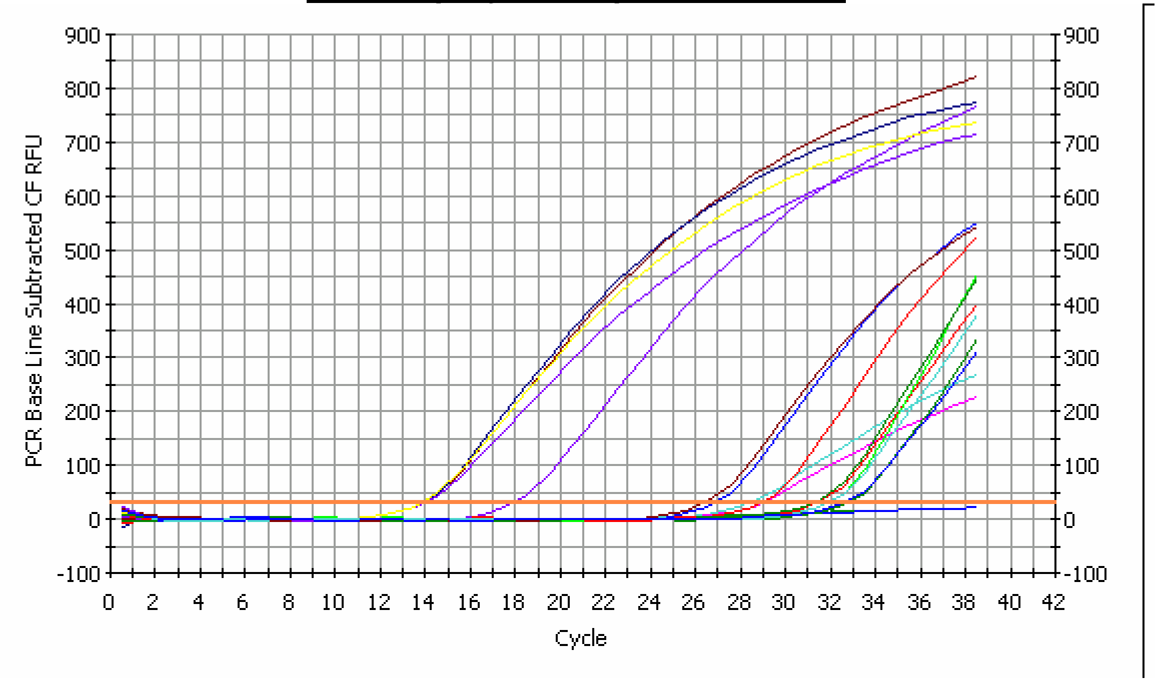

Data Analysis Parameters

Calculated threshold using the **maximum curvature approach** is **28.3**.
Per-well baseline cycles have been determined automatically.
Data analysis window is set at **95.00%** of a cycle, centered at **end** of the cycle.
Weighted Mean digital filtering has been applied. Global filtering is **off**.

PCR Quantification Spreadsheet Data for FAM-490

Well	Identifier	Ct	Setpoint
B01	2404n1	N/A	
B02	2405n1	28.3	
B03	240Tn1	26.7	
C01	2404n2	N/A	
C02	2405n2	28.8	
C03	240Tn2	26.3	
D01	2404a1	13.9	
D02	2405a1	13.8	
D03	240Ta1	17.9	
E01	2404a2	13.9	
E02	2405a2	13.8	
E03	240Ta2	31.3	
F01	2404n noRT	28.8	
F02	2405n noRT	31.8	
F03	240Tn noRT	31.2	
G01	2404a noRT	32.7	
G02	2405a noRT	31.8	
G03	240Ta noRT	32.5	

Mouse 256, 258-Tumor, and 258 MG

Current Date:	**09-Apr-08 06:54 PM**
Data generated on:	**09-Apr-08 at 03:57 PM**.
Optical data file name:	**Data 09-Apr-08 1557.opd**
Plate Setup file used:	**sassamples.pts**
Protocol file used:	**sasnisprobes.tmo**

PCR Amp/Cycle Graph for FAM-490

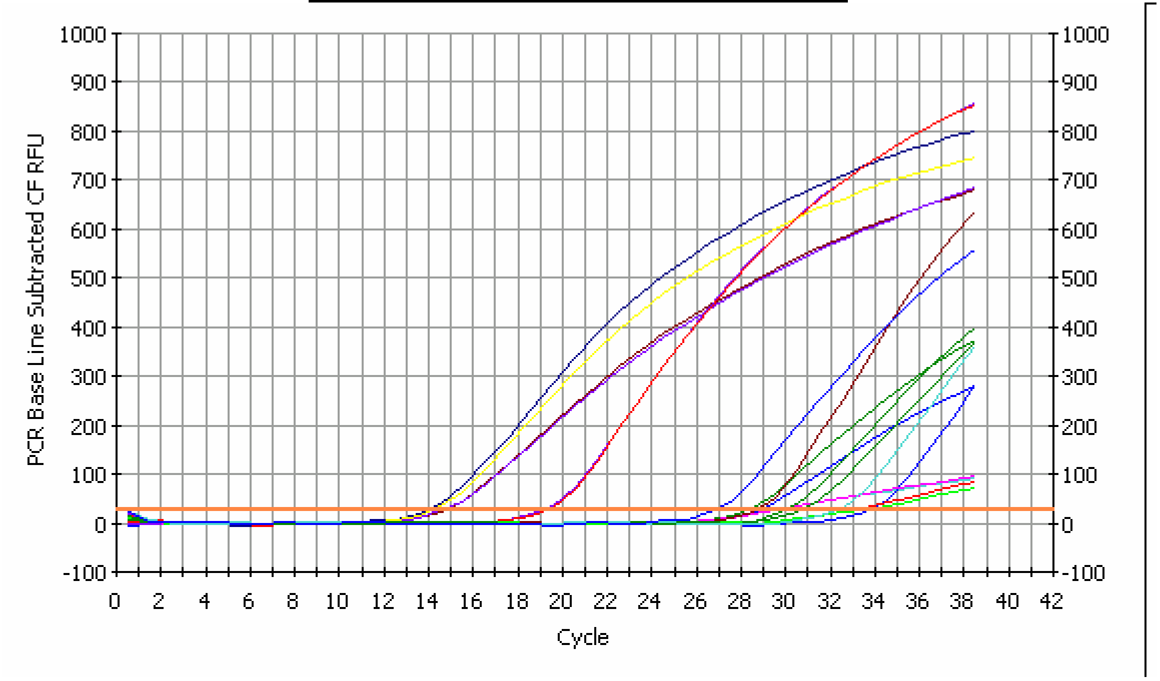

Data Analysis Parameters

Calculated threshold using the **maximum curvature approach** is **25.2**.
Per-well baseline cycles have been determined automatically.
Data analysis window is set at **95.00%** of a cycle, centered at **end** of the cycle.
Weighted Mean digital filtering has been applied. Global filtering is **off**.

PCR Quantification Spreadsheet Data for FAM-490

Well	Identifier	Ct	Setpoint
B01	256Mn1	28.2	
B02	258Tn1	29.6	
B03	258Mn1	33.7	
C01	256Mn2	28.8	
C02	258Tn2	29.3	
C03	258Mn2	28.6	
D01	256Ma1	14.7	
D02	258Ta1	13.9	
D03	258Ma1	19	
E01	256Ma2	14.6	
E02	258Ta2	14.2	
E03	258Ma2	19.1	
F01	256Mn noRT	32.8	
F02	258Tn noRT	32.9	
F03	258Mn noRT	29.9	
G01	256Ma noRT	30.6	
G02	258Ta noRT	32.2	
G03	258Ma noRT	26.7	

Mouse 251, 253, and 262

Current Date:	**11-Apr-08 01:03 AM**
Data generated on:	**10-Apr-08 at 11:35 PM**.
Optical data file name:	**Data 10-Apr-08 2335.opd**
Plate Setup file used:	**sassamples.pts**
Protocol file used:	**sasnisprobes.tmo**

PCR Amp/Cycle Graph for FAM-490

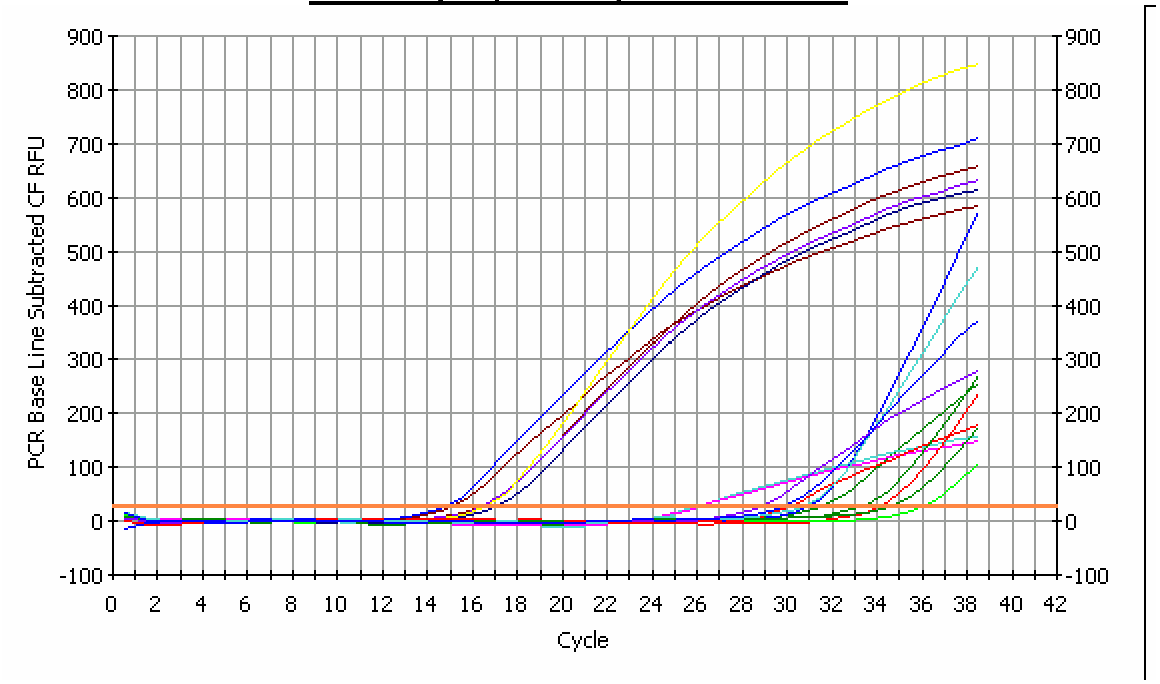

Data Analysis Parameters

Calculated threshold using the **maximum curvature approach** is **26.6**.
Per-well baseline cycles have been determined automatically.
Data analysis window is set at **95.00%** of a cycle, centered at **end** of the cycle.
Weighted Mean digital filtering has been applied. Global filtering is **off**.

PCR Quantification Spreadsheet Data for FAM-490

Well	**Identifier**	**Ct**	**Setpoint**
B01	251n1	31.5	
B02	253n1	25.9	
B03	262n1	14.7	
C01	251n2	30.9	
C02	253n2	26.1	
C03	262n2	15	
D01	251a1	16.4	
D02	253a1	17	
D03	262a1	28.8	
E01	251a2	16.4	
E02	253a2	16.5	
E03	262a2	30	
F01	251n noRT	34.1	
F02	253n noRT	35.9	
F03	262n noRT	34.6	
G01	251a noRT	33.2	
G02	253a noRT	30.7	
G03	262a noRT	29.8	

Mouse 209-2, 258MG, 251, and 240-4

Current Date:	**14-Apr-08 02:37 PM**
Data generated on:	**14-Apr-08 at 12:34 PM**.
Optical data file name:	**Data 14-Apr-08 1233.opd**
Plate Setup file used:	**sassamples2.pts**
Protocol file used:	**sasnisprobes.tmo**

PCR Amp/Cycle Graph for FAM-490

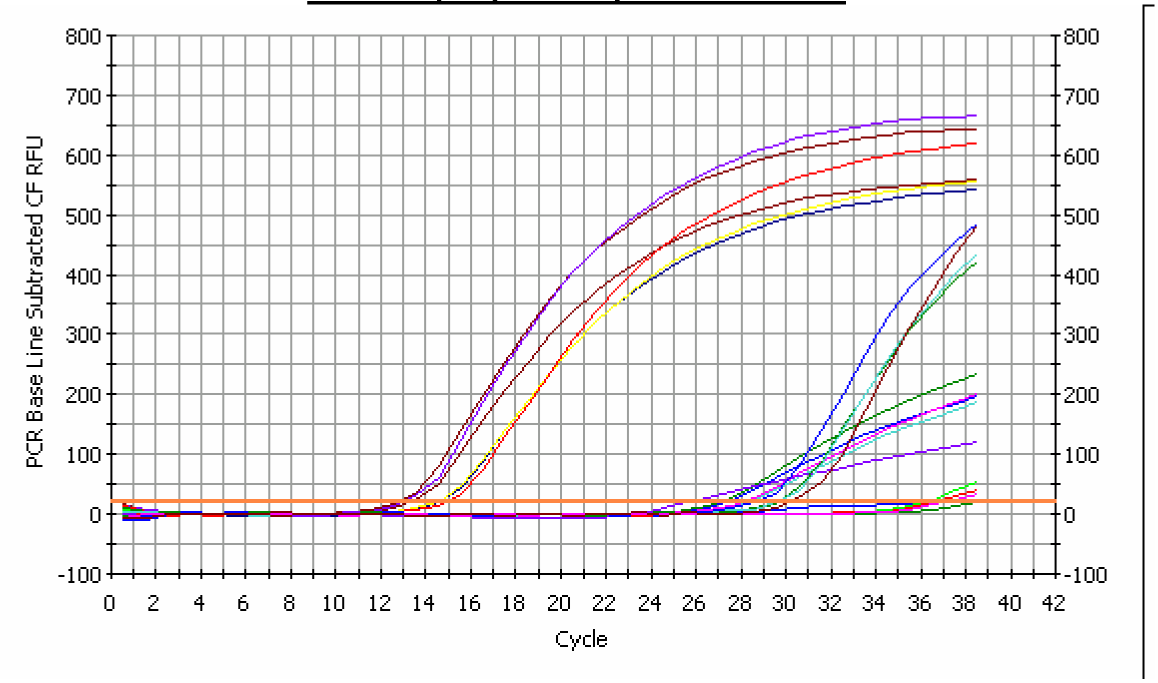

Data Analysis Parameters

Calculated threshold using the **maximum curvature approach** is **21.9**.
Per-well baseline cycles have been determined automatically.
Data analysis window is set at **95.00%** of a cycle, centered at **end** of the cycle.
Weighted Mean digital filtering has been applied. Global filtering is **off**.

PCR Quantification Spreadsheet Data for FAM-490

Well	Identifier	Ct	Setpoint
B01	209n1	27.1	
B02	258n1	28.4	
B03	240n	37.6	
C01	209n2	27.5	
C02	258n2	28.1	
C03	240a	12.8	
D01	209a1	13.4	
D02	258a1	14.6	
D03	251n	25.8	
E01	209a2	13.1	
E02	258a2	14.6	
E03	251a	15	
F01	209n noRT	36.8	
F02	258n noRT	36.4	
F03	240n noRT	N/A	
G01	209a noRT	29.7	
G02	258a noRT	29.7	
G03	240a noRT	28.7	
H02	251n noRT	37.3	
H03	251a noRT	30.2	

Mouse 209-2, 251, and 240-4

Current Date: **15-Apr-08 06:27 PM**
Data generated on: **14-Apr-08 at 05:10 PM**.

Optical data file name: **Data 14-Apr-08 1709.opd**
Plate Setup file used: **sassamples2.pts**
Protocol file used: **sasnisprobes.tmo**

PCR Amp/Cycle Graph for FAM-490

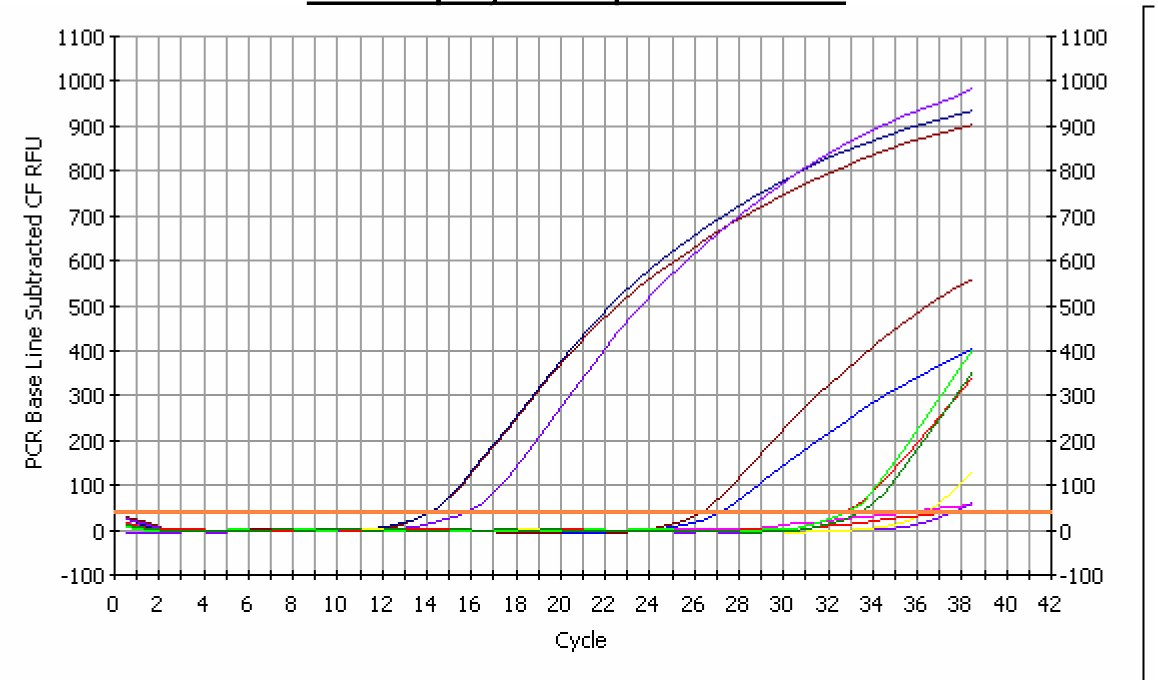

Data Analysis Parameters

Calculated threshold using the **maximum curvature approach** is **37.7**.
Per-well baseline cycles have been determined automatically.
Data analysis window is set at **95.00%** of a cycle, centered at **end** of the cycle.
Weighted Mean digital filtering has been applied. Global filtering is **off**.

PCR Quantification Spreadsheet Data for FAM-490

Well	Identifier	Ct	Setpoint
C01	209n	27	
C02	240n	35.1	
C03	251n	26.2	
D01	209a	14.1	
D02	240a	14	
D03	251a	15.7	
E01	209n no rt	37.5	
E02	240n no rt	36.3	
E03	251n no rt	37.1	
F01	209a noRT	32.6	
F02	240a noRT	32.6	
F03	251a noRT	33.3	

Mouse 250, 255, 261, and 240-Liver

Current Date:	**15-Apr-08 09:56 PM**
Data generated on:	**15-Apr-08 at 08:20 PM**.
Optical data file name:	**Data 15-Apr-08 2020.opd**
Plate Setup file used:	**sassamples3.pts**
Protocol file used:	**sasnisprobes.tmo**

PCR Amp/Cycle Graph for FAM-490

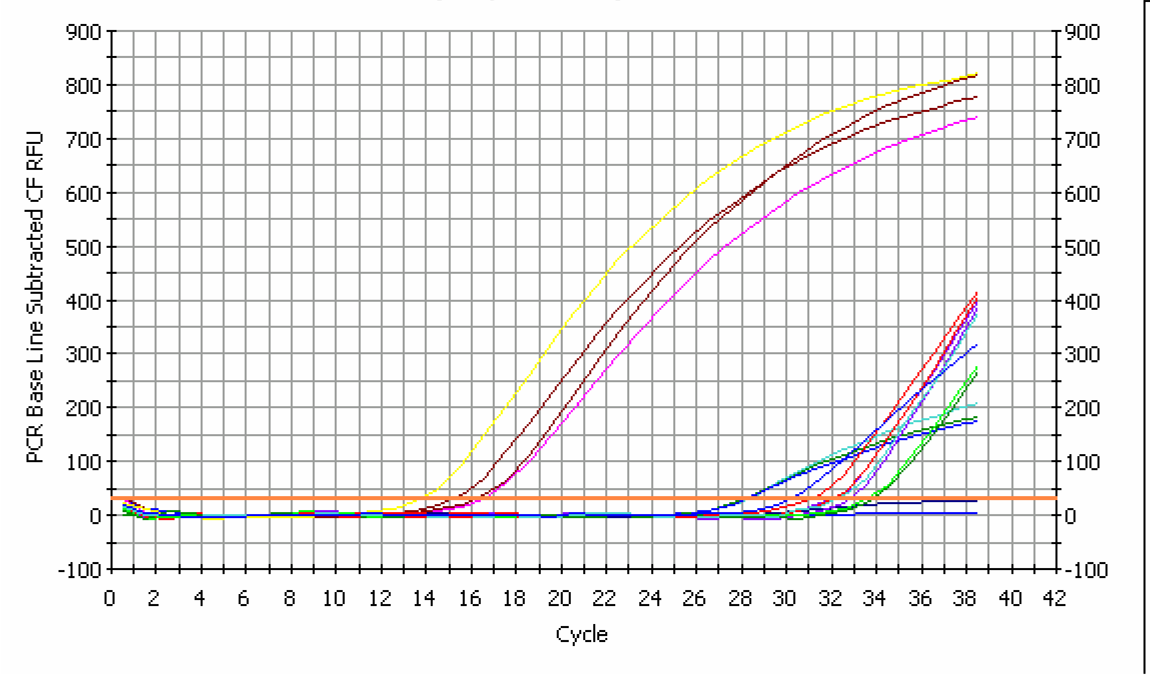

Data Analysis Parameters

Calculated threshold using the **maximum curvature approach** is **28.7**.
Per-well baseline cycles have been determined automatically.
Data analysis window is set at **95.00%** of a cycle, centered at **end** of the cycle.
Weighted Mean digital filtering has been applied. Global filtering is **off**.

PCR Quantification Spreadsheet Data for FAM-490

Well	Identifier	Ct	Setpoint
B01	250n1	27.9	
B02	255n	28.2	
B03	liv n	N/A	
C01	250n2	28	
C02	255a	16.4	
C03	liv a	16.1	
D01	250a	15.1	
D02	261n	N/A	
D03	liv n no rt	32.7	
E01	250n no rt	32	
E02	261a	13.7	
E03	liv a no rt	32	
F01	250a no rt	31	
F02	261n no rt	33.6	
F03	255n no rt	33.8	
G02	261a no rt	32.1	
G03	255a no rt	30.1	

Mouse 229, 251, 258Tumor

Current Date: **16-Apr-08 07:00 PM**
Data generated on: **16-Apr-08 at 04:50 PM**.

Optical data file name: **Data 16-Apr-08 1650.opd**
Plate Setup file used: **sassamples2.pts**
Protocol file used: **sasnisprobes.tmo**

PCR Amp/Cycle Graph for FAM-490

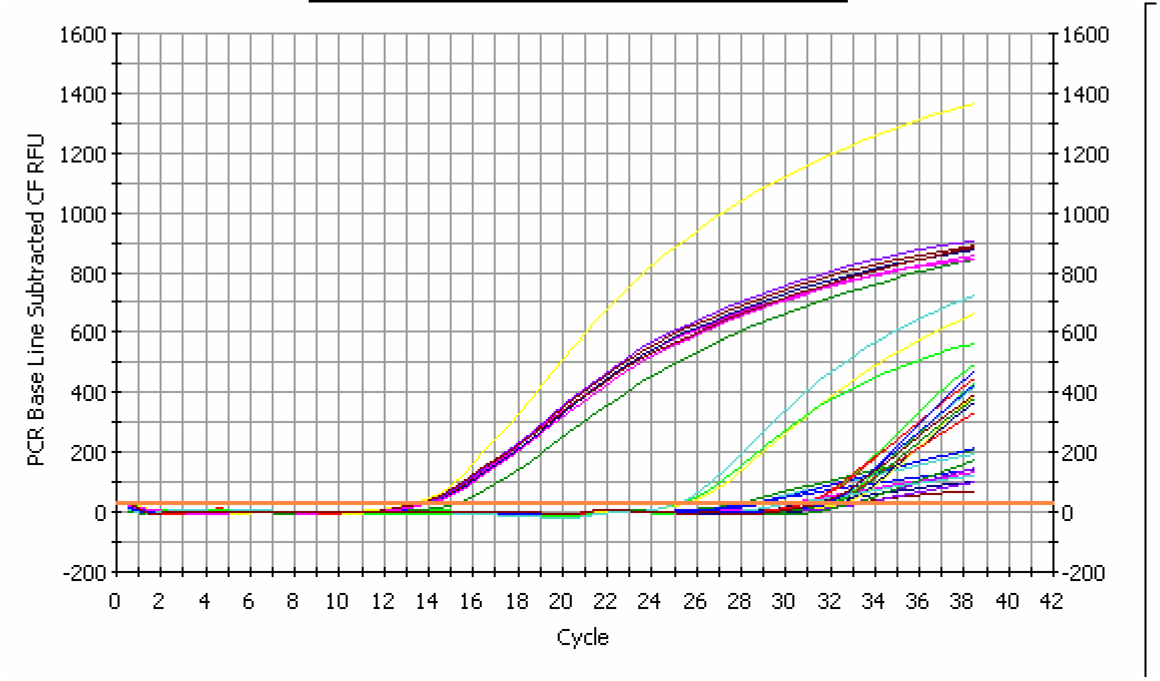

Data Analysis Parameters

Calculated threshold using the **maximum curvature approach** is **28.9**.
Per-well baseline cycles have been determined automatically.
Data analysis window is set at **95.00%** of a cycle, centered at **end** of the cycle.
Weighted Mean digital filtering has been applied. Global filtering is **off**.

PCR Quantification Spreadsheet Data for FAM-490

Well	Identifier	Ct	Setpoint
B01	T1A n1	27.9	
B02	T1B n	28.5	
B03	T2A n	29	
B04	T2B n	30.1	
B05	T3A n	32.8	
B06	T3B n	31	
C01	T1A n2	28.4	
C02	T1B a	13.9	
C03	T2A a	13.9	
C04	T2B a	13.9	
C05	T3A a	13.6	
C06	T3B a	13.2	
D01	T1A a	13.6	
D02	T1B n no rt	32.2	
D03	T2A n no RT	32.8	
D04	T2B n no RT	32.5	
D05	T3A n no RT	31.8	
D06	T3B n no RT	30.9	
E01	T1A n no rt	33.4	
E02	T1B a no RT	25.6	
E03	T2A a no rt	31	
E04	T2B a no RT	31.7	
E05	T3A a no RT	31.9	
E06	T3B a no RT	31.5	
F01	T1A a no rt	30.8	
F02	251n1	25.2	
F03	251n noRT	33	
F04	258n	30.4	
F05	258n no RT	31.7	
G01	251a	15.2	
G02	251n2	25.1	
G03	251a no rt	31.5	
G04	258a	14	
G05	258 a no rt	31.6	